Salinity effects on the mechanical behaviour of methane hydrate bearing sediments: a DEM investigation

Mingjing Jiang [a, b*], Ruohan Sun[a], Marcos Arroyo[c], Wenhao Du[d]

[a] *Department of Civil Engineering, School of Civil Engineering, Tianjin University, Tianjin 300072, China*

[b] *Department of Geotechnical Engineering, College of Civil Engineering, Tongji University, Shanghai 200092, China*

[c] *Departament of Civil and Environmental Engineering, Universitat Politècnica de Catalunya - BarcelonaTech, Jordi Girona 1-3, Barcelona 08034, Spain.*

[d] *Tongji Architectural Design (Group) Co., Ltd., No. 1230 Siping Road, Shanghai 200092, China. Former MSc student, Department of Geotechnical Engineering, College of Civil Engineering, Tongji University, Shanghai 200092, China*

[*] *Corresponding author.*

E-mail address: mingjing.jiang@tju.edu.cn;mingjing.jiang@tongji.edu.cn

Abstract.

The stability of methane hydrate depends on not only temperature and pressure but also the salinity of the environment where the methane hydrate exists. The variation in the stability of methane hydrate due to the change in salinity induces mechanical response in micro scale of the methane hydrate-bearing sediments (MHBS). However, it is really heard to quantitatively analyze this effect by controlling salinity of the MHBS in micro scale experiment. Therefore, our study applies Distinct Element Method to investigate the micro-scale mechanical response subject to the salinity variation. An existing contact model for cemented soils is extended to explicitly include the effects of salinity on bond strength and modulus, which are verified by experimental data. Using the proposed thermo-hydro-mechanical-chemical contact model, we conducted a series of case studies to investigate macroscopic and microscopic mechanical responses during three different stress paths, i.e. isotropic, triaxial and constant stress ratio tests. The results show that as the salinity increases, the shear strength and stiffness decrease while the deformation and bond breakage ratio accelerate. The results are valuable to develop constitutive models for MHBS and have safe exploitation of MH resources in the future.

Keywords: Distinct Element Method, Methane hydrate bearing sediments, Thermo-hydro-mechanical-chemical contact model, Salinity, Stress path.

1. Introduction

Methane hydrate (MH) is an ice-like crystalline consisting of methane molecules enclosed in a lattice of hydrogen-bonded water molecules (Soga et al., 2006; Sloan, 1998; Sloan, 2003; Waite et al., 2009). MHs have attracted major worldwide interest in recent years (Kvenvolden, 1988; Chong et al., 2016) as a future energy resource with potential to facilitate the transition of the global economy from conventional fossil fuels to renewable resources of energy.

In addition to its energy prospects, MH is considered as a geohazard trigger and has been linked with several historic submarine landslides (Uchida et al., 2012; Sultan et al., 2004; Huhn et al., 2019). This is because the dissociation of MH can lead to sediment weakening and instability (Hyodo et al., 2013; Wu et al., 2020a). This underlying feature also poses risks for energy production since most methods proposed for the recovery of methane from hydrate reservoir, via depressurization, thermal stimulation, chemical injection, etc. (Chong et al., 2016), face wellbore-instability problems. It is therefore imperative to characterize and understand the mechanical response of methane hydrate bearing sediments (MHBS) or energy soils (Jiang, 2019) under different conditions.

The mechanical behaviors of MHBS are largely influenced by the presence of MH. For instance, it is well established that the presence of hydrates leads to an increase in the strength and stiffness of the host sediment (Winters et al., 2004; Priest et al., 2005; Miyazaki et al., 2010; Ghiassian and Grozic, 2013; Hyodo et al., 2013; Hyodo et al.,

2013; Li et al., 2016; Sun et al., 2019; Wu et al., 2020b), which partly explains the engineering problems arising in practice from dissociation. To date, many laboratory tests have been performed on artificial or natural MHBS samples to quantify and correlate the influence on mechanical behaviour with several factors such as host sediment characteristics (Waite et al., 2009; Waite et al., 2004; Dai et al., 2012; Winters et al., 2014), hydrate formation morphology (Waite et al., 2004; Dai et al., 2012; Booth et al., 1996; Moridis et al., 2011; Malinverno and Goldberg, 2015; Masui et al., 2005); hydrate saturation (Hyodo et al., 2013; Masui et al., 2005; Yun et al., 2007; Miyazaki et al., 2011). These numerous influencing factors constitute a challenge to the design and interpretation of experimental studies. Such a challenge is magnified by the key role of environmental variables such as pressure and temperature conditions (Hyodo et al., 2013; Miyazaki et al., 2011; Hyodo et al., 2002; Hyodo et al., 2005; Li et al., 2012) as basic controls on dissociation onset. Ensuring the stability of methane hydrate as a solid requires a range of high pressure and low temperature conditions that raise significantly the cost and complexity of equipment in laboratory.

Pressure and temperature are not the sole environmental factors of significance. The temperature and pressure conditions ensuring hydrate stability depend also on environmental chemistry (Sloan and Koh, 2008). This feature was first noted in deep-water drilling, where hydrate formation is an impediment for drills and was fought against by using drilling fluids of high salt content (Halliday et al., 1998). The possibility of exploiting this phenomenon is now taken into serious consideration for methane recovery (Chong et al., 2016). The chemical injection method, i.e. to inject

chemicals, such as NaCl, methanol or ethylene glycol, to shift the hydrate pressure–temperature equilibrium conditions, is considered to be an effective gas hydrate dissociation method. However, although the effect of NaCl concentration on the phase-equilibrium and dissociation conditions of MH has been studied (Mimachi et al., 2016; Stern and Lorenson, 2014; Piramoon et al., 2019; Cha et al., 2016), the implications for the mechanical behaviour of MHBS of variable ambient salinities have not yet been explored. This salinity control will further increase the difficulty and cost in the experiments in laboratory. It seems therefore appropriate to start research on the topic with numerical analyses done by the Distinct Element Method (DEM) (Cundall and Strack, 1979).

The Distinct Element Method (DEM) (Cundall and Strack, 1979), which takes particles as the basic elements and allows multiscale study on granular materials, has been recently employed in the research on MHBS (Brugada et al., 2010; Jung, 2010; Jung et al., 2012; Vinod et al., 2014; He et al., 2016; Jiang et al., 2014). DEM has reproduced well-established experimental observations, e.g. the shear strength, small-strain stiffness and shear dilation of MHBS increase with the level of backpressure (Jiang et al., 2015), and decrease with the increasing of the temperature (Jiang et al., 2016; Jiang et al., 2017). In addition, DEM studies of MHBS may go beyond current capabilities in laboratory on many aspects. For instance, examination on the mechanical behaviour of MHBS has been almost always limited to conventional triaxial compression tests or direct shear tests in laboratory (Santamarina et al., 2015; Liu et al., 2017; Kato et al., 2016). However, the stress paths anticipated during engineering

activities such as sampling MH from sediment layers, well construction, and multi-phase flow during MH dissociation are very complicated and different from those in conventional tests. The unsatisfactory situation constrains not only the understanding of MHBS mechanical behaviour but also its constitutive model development, since the mechanical behaviour of soils under a wide range of stress paths is crucial to develop their constitutive models (Xiao et al., 2015).

Previous studies have shown that the effects are large on mechanical properties of MHBS when MH is cemented with soil particles (Masui et al., 2005; Hyodo et al., 2009), therefore, this paper will focus on this cementation-type MHBS. A well-established three-dimensional (3D) bond contact model for MHBS (Shen et al., 2016; Shen and Jiang, 2016; Jiang et al., 2014; Jiang et al., 2015; Jiang et al., 2015; Shen et al., 2016; Jiang et al., 2019) is here generalized to take into account the effect of salinity on MH behaviour, which gives rise to a novel thermo-hydro-mechanical-chemical (THMC) bond contact model accounting for the influences of ambient temperature, pore water pressure, and salinity on the mechanical behaviour of MHBS. In what follows, the model characteristics are first introduced in detail with emphasis on the incorporation of salinity effects. The model was implemented in a DEM commercial code and the necessary calibration and validation to represent MHBS are then explained. Finally, we present and discuss DEM simulation results in which the new model is employed to explore the effect of salinity on MHBS response along different stress paths.

2. A THMC contact model for MHBS

Shen and Jiang (2016) established and validated a bond contact model for MHBS built upon the complete unbonded contact model proposed by Jiang et al. (2015) and a bond contact element proposed by Shen et al. (2016). The DEM incorporating this model is able to describe the mechanical behaviour of MHBS with its dependency on MH habits, i. e. coating or cementing, density, saturation, temperature, and water pressure without taking into account the complex effect of salinity on hydrate bonds. Thus, this paper will extend this existing model to the THMC problem. In this section, we first describe briefly the fundamental characteristics of the mechanical model (i.e. force–displacement law, bond failure criterion, bond geometry and hydrate saturation), and then how temperature, pressure and salinity effects are considered in the model.

2.1 Force-displacement law

The bond contact model (Shen et al., 2016) regards the transmission of forces at contact as a combination of two parts: the particle contact part and the MH bond contact part, which can be expressed as follows::

$$\boldsymbol{F}_{\mathrm{n}} = \boldsymbol{F}_{n,p} + \boldsymbol{F}_{n,b} \tag{1}$$

$$\boldsymbol{F}_{\mathrm{s}} = \boldsymbol{F}_{s,p} + \boldsymbol{F}_{s,b} \tag{2}$$

$$\boldsymbol{M}_{\mathrm{r}} = \boldsymbol{M}_{r,p} + \boldsymbol{M}_{r,b} \tag{3}$$

$$\boldsymbol{M}_{\mathrm{t}} = \boldsymbol{M}_{t,p} + \boldsymbol{M}_{t,b} \tag{4}$$

where $\boldsymbol{F}n$, $\boldsymbol{F}s$, $\boldsymbol{M}r$, and $\boldsymbol{M}t$ are the total normal force due to compression/ tension, shear force due to relative tangential displacement, bending moment due to rolling angle, and torque due to twisting angle at each contact, respectively. $\boldsymbol{F}n,p$, $\boldsymbol{F}s,p$, $\boldsymbol{M}r,p$, and $\boldsymbol{M}t,p$ denote the normal force, tangential force, rolling moment and torque sustained by particles, respectively with subscript p representing particle. $\boldsymbol{F}n,b$, $\boldsymbol{F}s,b$, $\boldsymbol{M}r,b$, and $\boldsymbol{M}t,b$ are those by MH bond part respectively with subscript b representing bond. A grain in MHBS is simplified as a sphere in the work and the bond material is idealized in shape as a cylinder with concave ends complementary with the surfaces of the two bonded spheres. The effect of such bond geometry is considered in terms of bond strength and stiffness. Note that the bond contact behaviour after bond breakage is assumed to be controlled by the microscopic contact model for unbonded contact, which indicate that there is no bond residue to interact with sphere particles. Thus, any possible effect of fragmented or adhered bond material is neglected on the mechanical behaviour of the MHBS. Table 1 summarizes the mechanical responses assumed in the model in each direction, whereas Table 2 presents the key formulae. Further details are available in (Shen et al., 2016).

Table 1 Mechanical responses of bonded grains in the model

Bonded grains	Normal direction	Tangential direction	Rolling direction	Twisting direction
Particle 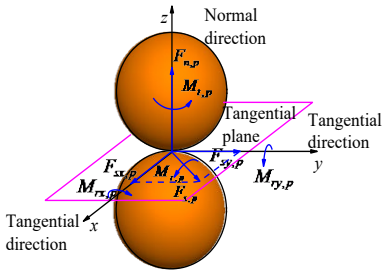	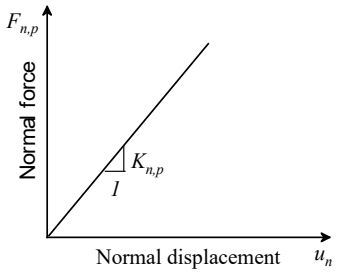	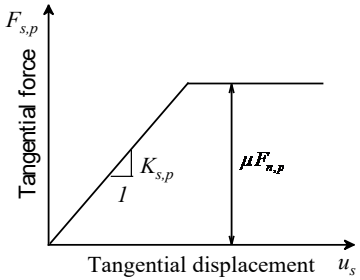	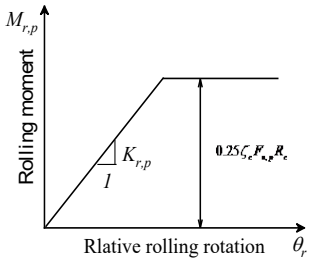	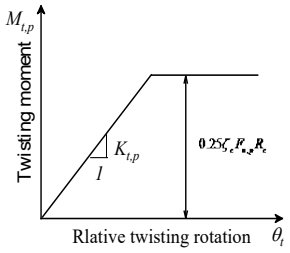
Bond 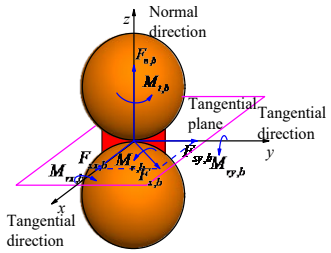	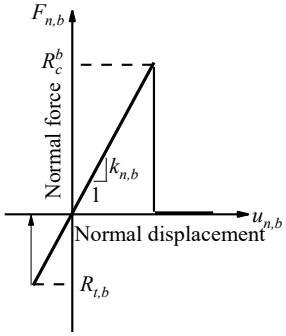	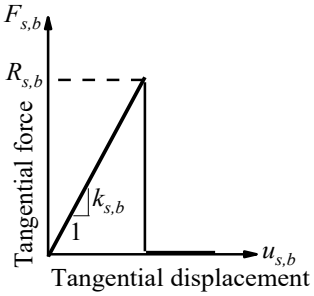	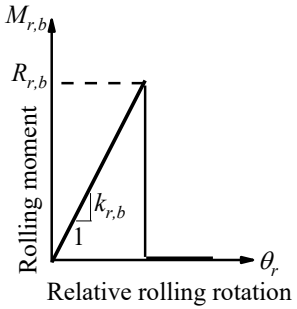	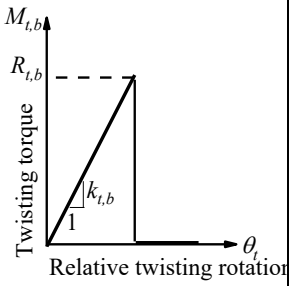

Table 2 Summary of the key formulae controlling the mechanical behaviour of bonded grains

		Contact response	Stiffness	Peak resistance
Particle part	Normal	$\boldsymbol{F}_{n,p} = K_{n,p} u_n \boldsymbol{n}$	$K_{n,p} = 2E_p R$	—
	Tangential	$\boldsymbol{F}_{s,p} \leftarrow \boldsymbol{F}_{s,p} + K_{s,p} \dot{\boldsymbol{u}}_s \Delta t$	$K_{s,p} = K_{n,p} / \xi$	$\mu F_{n,p}$
	Rolling	$\boldsymbol{M}_{r,p} \leftarrow \boldsymbol{M}_{r,p} + K_{r,p} \dot{\boldsymbol{\omega}}_r \Delta t$	$K_{r,p} = 0.25 K_{n,p} R_c^2$	$0.25 \zeta_c F_{n,p} R_c$
	Torsional	$\boldsymbol{M}_{t,p} \leftarrow \boldsymbol{M}_{t,p} + K_{t,p} \dot{\boldsymbol{\omega}}_t \Delta t$	$K_{t,p} = 0.5 K_{s,p} R_c^2$	$0.65 \mu F_{n,p} R_c$
Bond part	Normal	$\boldsymbol{F}_{n,b} \leftarrow \boldsymbol{F}_{n,b} + K_{n,b} \dot{\boldsymbol{u}}_n \Delta t$	$K_{n,b} = \frac{F_{n,b}}{\delta} = \frac{\pi E_b D_b n}{2} \left[l \ln\left(l - \frac{\sqrt{n^2-1}}{n} \right) + \frac{\sqrt{n^2-1}}{n} - l \ln(l-1) - 1 \right]$	$R_{nt} = \sigma_t A_b$ $R_{nc} = \sigma_c A_b$
	Tangential	$\boldsymbol{F}_{s,b} \leftarrow \boldsymbol{F}_{s,b} + K_{s,b} \dot{\boldsymbol{u}}_s \Delta t$	$K_{s,b} = K_{n,b} / 2(1+\nu_b)$	Eqs. (7-9)
	Rolling	$\boldsymbol{M}_{r,b} \leftarrow \boldsymbol{M}_{r,b} + K_{r,b} \dot{\boldsymbol{\omega}}_r \Delta t$	$K_{r,b} = \frac{M_{r,b}}{\theta_r} = \frac{\pi E_b D_b^3 n^3}{16} \left\{ \frac{1}{3}\left[1 - \frac{(n^2-1)^{1.5}}{n^3} \right] + \frac{m^2+2mn}{n^2}\left(1 - \frac{\sqrt{n^2-1}}{n} \right) + \frac{m+n}{2n^3} + \frac{m^3+3m^2n+2mn^2}{n^3}\left[\ln(l-1) - \ln\left(l - \frac{\sqrt{n^2-1}}{n} \right) \right] \right\}$	
	Torsional	$\boldsymbol{M}_{t,b} \leftarrow \boldsymbol{M}_{t,b} + K_{t,b} \dot{\boldsymbol{\omega}}_t \Delta t$	$K_{t,b} = K_{r,b} / 1+\nu_b$	

In Table 2, u_n denotes inter-particle overlap, E_p the modulus of the particle material, R the harmonic mean of the particle radii, ξ the ratio of normal stiffness over tangential stiffness, μ the inter-particle friction coefficient, R_c the radius of contact area, and ζ_c the effect of local asperity crushing (hereafter this effect is not considered and $\zeta_c = 4$). Δt denotes the time step used in the DEM computations. $\boldsymbol{n}$ is a unit vector in the contact normal direction, $\dot{\boldsymbol{u}}_n$, $\dot{\boldsymbol{u}}_s$, $\dot{\boldsymbol{\omega}}_r$, and $\dot{\boldsymbol{\omega}}_t$ are the relative normal velocity, tangential velocity, rolling rate and torsional rate at a contact, respectively. D_b, w_{MH}, and h_{min} denote the particle diameter, bond cylinder diameter and the minimum thickness of the bond cylinder in height, respectively, which will be further illustrated in Fig. 3. E_b is the Yong's modulus of the bond material, and δ the change of the bond cylinder in height. $m = h_{\min}/w_{MH}$ namely bond slenderness ratio, and $n = D_b/w_{MH}$ two dimensionless quantities characterizing the geometry of a bond cylinder, and $l = m/n + 1$. ν_b is the Poisson's ratio of the bond material, and θ_r the rolling rotation, σ_t and σ_c the tensile and compression strengths of bond material respectively. R_{nt}, R_{nc}, $R_{s,b}$, $R_{r,b}$, $R_{t,b}$ represent tensile, compressive, shear, bending and torsional resistance, respectively.

2.2 Bond failure criterion

The 3D bond failure criterion used is able to describe the combining effect of normal force, shear force, rolling moment, and torque on bond failure, in association with bond geometry. Although good results have been obtained in DEM simulations (Jiang et al., 2019) where a numerically developed bond failure criterion (Shen et al., 2016) was used, we shall use experimentally-validated criterion in this work. A 2D failure criterion

was first obtained experimentally from tests on pairs of rods bonded with cement or epoxy resin (Jiang et al., 2012), and then a 3D criterion obtained on spheres bonded with cement (Jiang et al., 2015; Jin, 2016), from which an ellipsoidal 3D bonded strength envelope can be proposed. Fig. 1 presents the bond strength envelope obtained from 3D experiments (Jiang et al., 2015; Jin, 2016) and used in this study..

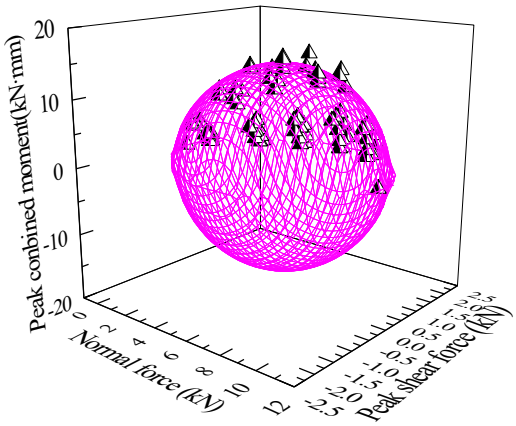

Fig. 1 Bond strength envelope obtained from 3D experiments (data adapted from [61])

This envelope can be practically described as follows:

$$\left(\frac{\|\boldsymbol{F}_{s,b}\|}{R_{s,b}}\right)^2+\left(\frac{\|\boldsymbol{M}_{r,b}\|}{R_{r,b}}\right)^2+\left(\frac{\|\boldsymbol{M}_{t,b}\|}{R_{t,b}}\right)^2\begin{cases}<1 & \text{Intact}\\ =1 & \text{Critical}\\ >1 & \text{Broken}\end{cases} \tag{5}$$

The criterion includes five basic modes, i.e. tension, compression, shear, bending and torsion, which can be calculated respectively according to the following formulas:

$$R_{nt}=\sigma_t A_{\mathrm{b}}\,,\ R_{nc}=\sigma_{\mathrm{c}} A_{\mathrm{b}} \tag{6a,b}$$

$$R_{s,b}=0.145\times\sqrt{\left(R_{nt}+R_{nc}\right)^2-\left(2\boldsymbol{F}_{n,b}-R_{nc}+R_{nt}\right)^2} \tag{7}$$

$$R_{r,b}=0.175\times R_{\mathrm{b}}\times\sqrt{\left(R_{nt}+R_{nc}\right)^2-\left(2\boldsymbol{F}_{n,b}-R_{nc}+R_{nt}\right)^2} \tag{8}$$

$$R_{t,b}=0.189\times R_{\mathrm{b}}\times\sqrt{\left(R_{nt}+R_{nc}\right)^2-\left(2\boldsymbol{F}_{n,b}-R_{nc}+R_{nt}\right)^2} \tag{9}$$

where σ_t and σ_c are the tensile and compression strengths of bond material respectively. $A_b = \pi R_b^2$ is the section area of bond cylinder.

2.3 Bond geometry and hydrate saturation

Although the model proposed by Shen & Jiang (Shen and Jiang, 2016; Jiang et al., 2019) can also address hydrate coating, this work will only deal with cementation-type MHBS, in which hydrate exists in the form of cementation between soil particles. An image illustrating the formation of cementation-type hydrate is reproduced in Fig. 2. Fig. 2 shows that the water added previously was mainly distributed between the grains (in red color) as a meniscus at the contacts. The methane hydrate formed was roughly in that shape after a span of time under certain temperature and pressure conditions maintained, and cemented the neighbouring grains firmly.

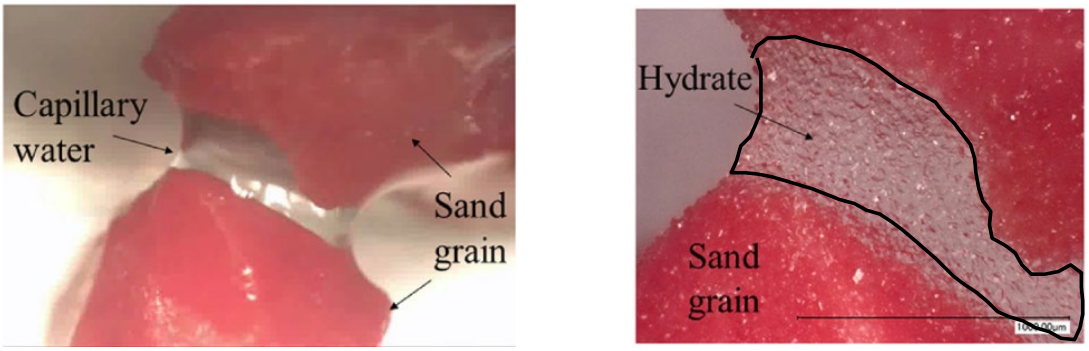

Fig. 2 Formation of methane hydrate between grain contacts under Electron Scanning Microscope[62]

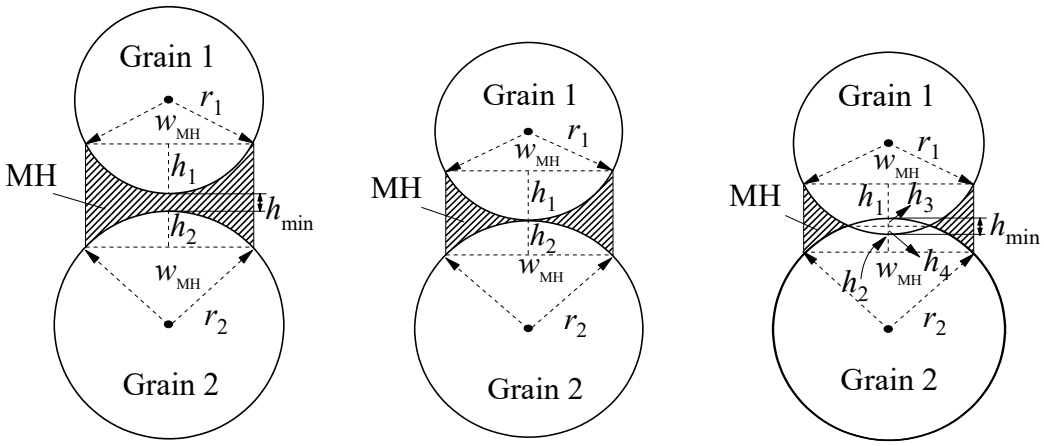

(a) $h_{min} > 0$ (b) $h_{min} = 0$ (c) $h_{min} < 0$

Fig. 3 Geometry of cementation-type MH morphology

In the model, the width of the cementation-type hydrate bond or bond cylinder diameter w_{MH} is assumed proportional to the radius of the contacting particles, r_1 and r_2, as $w_{MH} = 2R_b = 2\lambda\overline{R}$, where R_b is the bond cylinder radius and $\overline{R} = \min[r_1, r_2]$. The proportionality constant λ is termed as the hydrate radius multiplier in this paper. As shown in Fig. 3, there are three types of bond according to the quantity of the minimum cementation thickness h_{min}, i.e. h_{min} >0, =0, <0. If all bonds have $h_{min} \geq 0$, as illustrated in Fig. 3 (a) and (b), the total volume of hydrate cementation V_{MH} can be calculated as follows:

$$V_{MH} = \sum_{N_c} [\pi R_b^2 (h_{min} + h_1 + h_2) - \pi h_1^2 (r_1 - h_1/3) - \pi h_2^2 (r_2 - h_2/3)] \tag{10}$$

where,

$$h_1 = r_1 - \sqrt{r_1^2 - R_b^2}\,,\ h_2 = r_2 - \sqrt{r_2^2 - R_b^2} \tag{11a,b}$$

When $h_{min} < 0$ as shown in Fig. 3 (c), V_{MH} can be calculated by summing up the volume at all the relevant contacts as follows:

$$V_{MH} = \sum_{N_c} [\pi R_b^2 (h_{min} + h_1 + h_2) - \pi h_1^2 (r_1 - \frac{h_1}{3}) - \pi h_2^2 (r_2 - \frac{h_2}{3}) + \pi h_3^2 (r_2 - \frac{h_3}{3}) + \pi h_4^2 (r_1 - \frac{h_4}{3})] \tag{12}$$

where $h_3 = r_2 - \dfrac{r_2^2 - r_1^2 + d^2}{2d}$, $h_4 = r_1 - \dfrac{r_1^2 - r_2^2 + d^2}{2d}$, $d = h_1 + h_2 - h_3 - h_4$ (13a,b,c)

In a general case, in which the specimen is characterized with the three-types contacts, V_{MH} is computed by summing up the volume of bonds in each type. In all cases, MH saturation S_{MH} is defined as follows:

$$S_{MH} = \frac{V_{MH}}{V_V} \tag{14}$$

where V_v is the total volume of void in MHBS. In general, V_{MH} is controlled by particle size distribution, fabric at the moment of bonding, and the value of the hydrate radius multiplier λ. For a given collection of particles in a DEM specimen, V_{MH} is uniquely linked to S_{MH} through λ in the work.

2.4 Thermo-hydro-chemical effects on bond properties

2.4.1 Effects of temperature and pressure

For given chemical conditions, pressure and temperature control the stability of methane hydrates. The stability boundary line, i.e. phase-equilibrium line, is the locus of conditions out of which dissociation takes place. Hyodo et al. (2005) proposed a parameter L, defined as the minimum distance between a test condition point and the stability boundary line of MH, to describe the effects of the temperature and pressure on MH mechanical behaviour.

Fig. 4 illustrates the stability boundary of MH on a normalized temperature-pressure plane. To facilitate the link to salinity effects later, the normalized quantities are hereafter defined as $T^* = T_0/T$ and $P^* = P/P_0$, where $T[\mathrm{K}]$ is temperature in Kelvin scale, P_0 = 2.23 MPa and T_0 = 273 K represent the intersection point at which two boundary lines meet for MH phase equilibrium in pure water. On this T^*-P^* plane, the stability boundary is given by

$$\ln(P/P_0)=\begin{cases}-35\times(T_0/T)+35 & T\geq T_0\\ -7.5\times(T_0/T)+7.5 & T<T_0\end{cases} \tag{15}$$

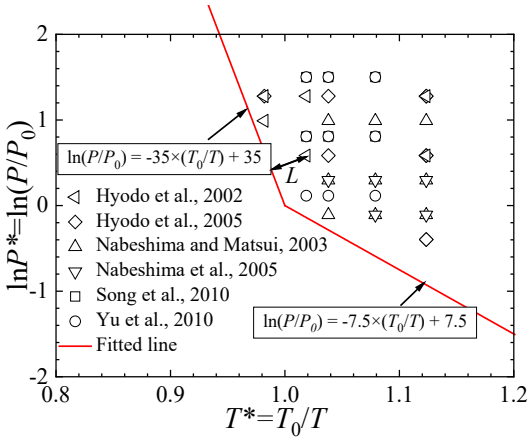

Fig. 4. Test conditions and phase equilibrium line of methane hydrate.

Fig. 4 also contains the data on test conditions in which the MH strength $q_{\max}$ can be obtained from the literature (Hyodo et al., 2002; Hyodo et al., 2005; Nabeshima and Matsui, 2003; Nabeshima et al., 2005; Song et al., 2010; Yu et al., 2010), where $q=\sigma_1-\sigma_3$ in triaxial compression test. For each of them, parameter L is computed and plotted against the measured strength in Fig. 5. Despite some scatter, an increasing trend of $q_{\max}$ is observed against L. A linear relationship can be used to describe the trend with a slope of 69.38MPa as follows:

$$q_{\max}=69.38\times L(T,P) \tag{16}$$

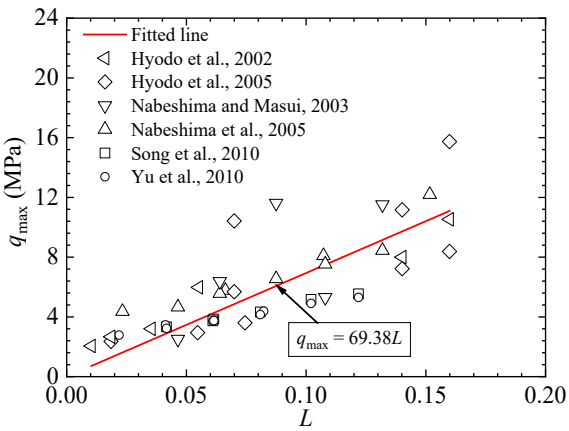

Fig. 5 Relationship between methane hydrate peak strength and parameter L

Because it is difficult to obtain the initial elastic modulus of MH E_{MH} accurately in laboratory, the secant modulus E_{50} is used to represent its elasticity, which is defined as the ratio of stress over strain where one half of the peak stress is mobilized. Fig. 6 presents the relationship between E_{50} and L, whose data comes from (Hyodo et al., 2002; Hyodo et al., 2005; Nabeshima and Matsui, 2003; Nabeshima et al., 2005; Song et al., 2010). Generally, the secant modulus increases with L, and a linear relationship can be approximated with a slope of 888.78 MPa as follows:

$$E_{50} = 888.78 \times L + 150.49 \tag{17}$$

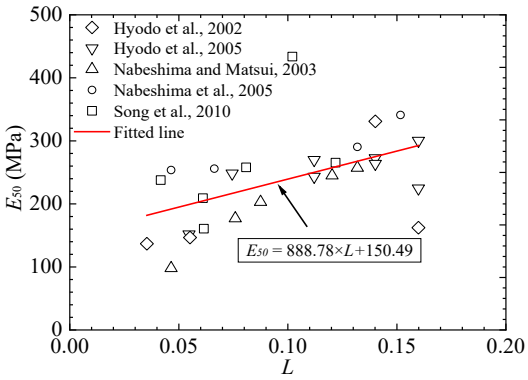

Fig. 6 Relationship between MH modulus and parameter L

2.4.2 Effect of salinity

NaCl is one of the main components in seawater, with which the MH in natural seabed coexists (Priest et al., 2005). Previous research has shown that NaCl can shift the position of MH phase equilibrium line. Fig. 7 summarizes the experimental data on MH phase equilibrium on temperature–pressure scale where NaCl solution has different value of concentrations (Cha et al., 2016; Maekawa, 2001; Dholabhai et al., 1991; Jager and Sloan, 2001; Kharrat and Dalmazzone, 2003; Lu and Matsumoto, 2005; Lafond et al., 2012; Sylva et al., 2016; Sun et al., 2011).

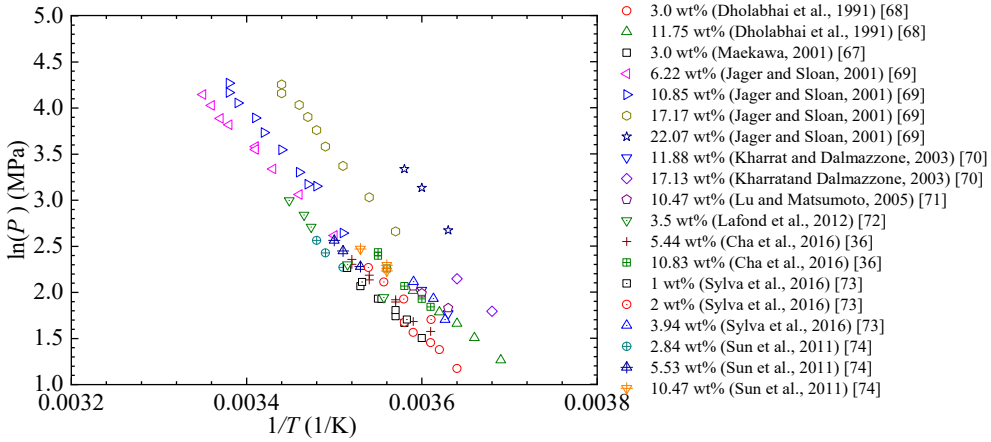

Fig. 7 Experimental data on MH phase equilibrium on temperature-pressure scale where NaCl solution has different concentration value

These data can be normalized and categorized into six series with different values of concentration: 3 wt%, 6 wt%, 11 wt%, 17 wt%, 22 wt % and 24 wt%, as shown in Fig. 8. Fig. 8 shows that, the hydrate phase equilibrium lines in different NaCl concentration are all substantially parallel to the phase equilibrium line in pure water (i.e. the line shown in Fig. 4). As the NaCl concentration increases, the MH phase equilibrium line shifts gradually to the right side on the normalized temperature–pressure scale, which reduces the temperature and increases the pressure required for the stability. This will lead to the fact that in any given condition on pressure and temperature, different value of NaCl concentration makes the MH have different value of L. Therefore, if we describe the shift of the phase equilibrium line as a function of salinity w, the chemical factor can be naturally introduced to control the mechanical behaviour of MH and then a THMC contact model for MHBS will be established.

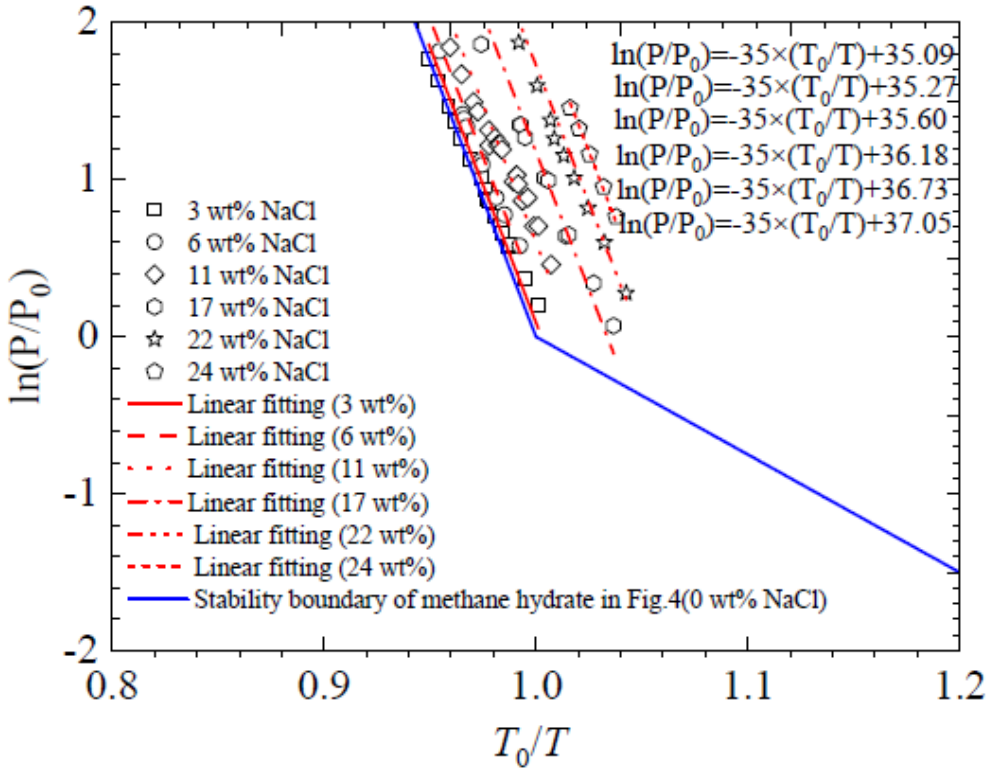

Fig. 8 Normalized MH phase equilibrium line in different NaCl concentration with data from (Cha et al., 2016; Maekawa, 2001; Dholabhai et al., 1991; Jager and Sloan, 2001; Kharrat and Dalmazzone, 2003; Lu and Matsumoto, 2005; Lafond et al., 2012; Sylva et al., 2016; Sun et al., 2011).

In the previous sub-section, a bilinear approximation was proposed for the phase equilibrium line on the T^*-P^* plane in Fig. 4, with the intersection point of the two lines denoted as (T_0, P_0). Although more data is certainly needed on the phase equilibrium in Fig. 8 to describe complete bi-linear equilibrium lines at different value of NaCl concentration, it is here assumed that they have the identical P_0 value but different T_0 value, as shown in Fig. 9.

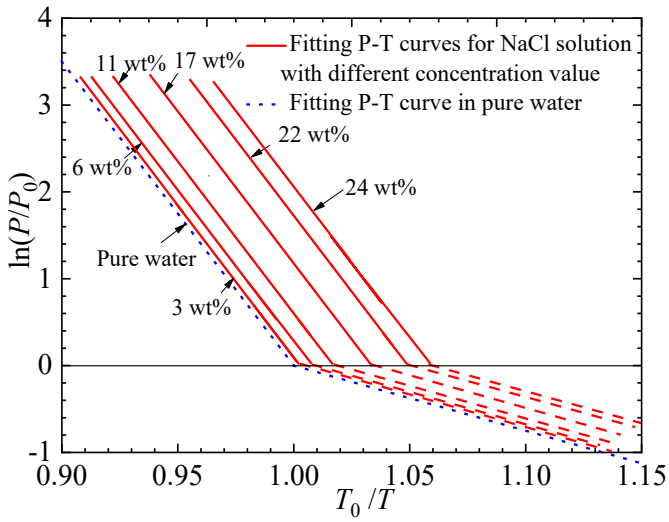

Fig. 9 Phase equilibrium lines suggested for MH in different concentration of salt solution

Consequently, the phase equilibrium line of MH at different NaCl solution is described by Eq. (18):

$$\ln(P/P_0)=\begin{cases}-35\times(T_0/T)+a & T\le T_0\\ -7.5\times(T_0/T)+b & T>T_0\end{cases} \tag{18}$$

where the influence of salinity w on the phase equilibrium line of MH is controlled by parameters a and b. This influence is described quantitatively in Fig. 10 and can be expressed by the following equations:

$$a/a_0=0.00059\times(w/w_0)^2+0.00253\times(w/w_0)+1 \tag{19}$$

$$b/b_0=0.00059\times(w/w_0)^2+0.00253\times(w/w_0)+1 \tag{20}$$

where $a_0 = 35$ and $b_0 = 7.5$ are the values corresponding to the MH equilibrium line in pure water, and w_0 is the average salinity of seawater in the world, i.e. $w_0 = 3$ wt%.

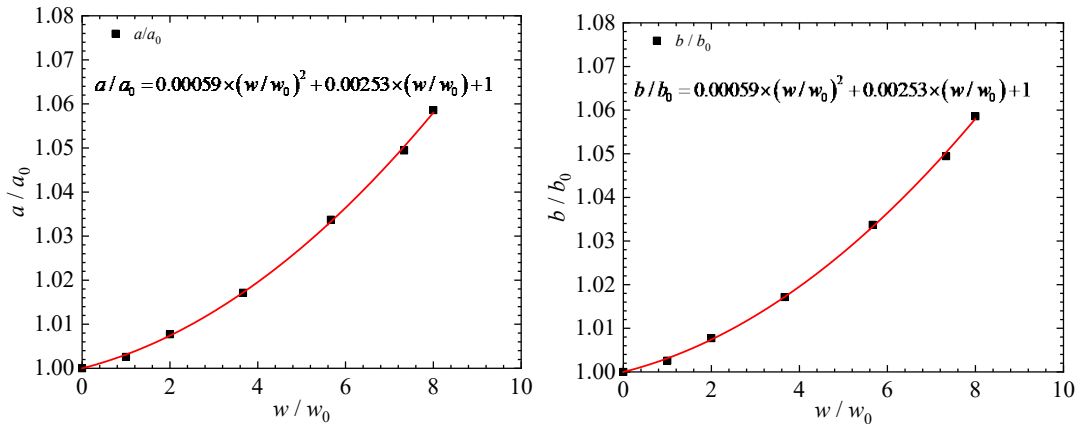

(a) Normalized *a*-*w* relationship (b) Normalized *b*-*w* relationship

Fig. 10 The relationship between parameters *a*, *b* and salinity solution *w*

In order to increase computation efficiency, the whole normalized temperature - pressure plane can be divided into three zones as shown in Fig. 11. In the figure, BD is the angle bisector separating Zones I and II. Line AB is used to calculate L in Zone I while line BC for *L* in Zone II. In contrast, MH would dissociate in Zone III. Thus, parameter *L*, which is hereafter temperature, pressure and salinity dependent, can be calculated by Eq. (21).

$$L=\begin{cases}\left|35\times(T_0/T)+\ln(P/P_0)-35\times\left[0.00059\times(w/w_0)^2+0.00253\times(w/w_0)+1\right]\right| \Big/ \sqrt{3.5^2+1^2} & \text{Zone I}\\ \left|7.5\times(T_0/T)+\ln(P/P_0)-7.5\times\left[0.00059\times(w/w_0)^2+0.00253\times(w/w_0)+1\right]\right| \Big/ \sqrt{7.5^2+1^2} & \text{Zone II}\\ 0 & \text{Zone III}\end{cases}$$

(21)

which can be further simplified as

$$L=\begin{cases}9.615\times(T_0/T-1)+0.27\times\ln(P/P_0)-5.673\times10^{-3}\times(w/w_0)^2-2.4\times10^{-2}\times(w/w_0) & \text{Zone I}\\ 0.991\times(T_0/T-1)+0.132\times\ln(P/P_0)-5.848\times10^{-4}\times(w/w_0)^2-2.508\times10^{-3}\times(w/w_0) & \text{Zone II}\\ 0 & \text{Zone III}\end{cases}$$

(22)

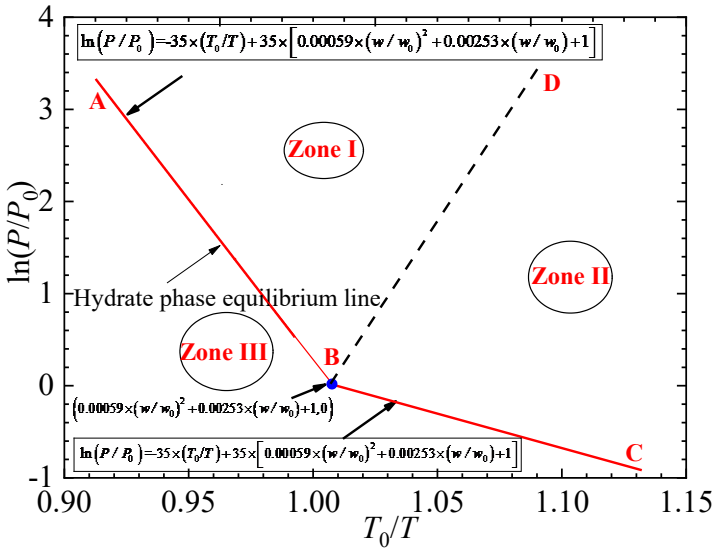

Fig. 11 Equilibrium lines of hydrate phase and temperature and pressure conditions in the test

The link between bond strengths and ambient TH conditions was established in previous work (Jiang et al., 2014; Shen and Jiang, 2016) since the ambient pore water pressure (or *back pressure*) in a MHBS specimen plays a role on the MH bond similar to the confining pressure (P) acting on a pure MH specimen in triaxial test. Thus, in this study, compression strength σ_c and tension strength σ_t of the MH bond can be formulated as folloωs:

$$\begin{aligned} \sigma_{\mathrm{c}} &\rightarrow \sigma_{c,f} - P = q_{\max} = \alpha_s 69.38 \times L(T,P,w) \\ \sigma_{\mathrm{t}} &\rightarrow P - \sigma_{t,f} = \alpha_s 69.38 \times L(T,\sigma_{t,f},w) \end{aligned} \tag{23}$$

where $\sigma_{c,f}$ is the peak major principal stress and $\sigma_{t,f}$ is the peak minor principal stress, α_s is a size-effect correction coefficient which will be introduced later.

3. Model calibration and validation

The THMC bond contact model presented above was implemented into a commercial DEM software, PFC3D (Itasca, 2015) by using a C++ subroutine, which was then used to simulate triaxial compression tests on MHBS for validation. The

parameters and their values used in the simulations are listed in Table 3. The values for particle part were those in previous DEM studies (Shen and Jiang, 2016; Jiang et al., 2015; Jiang et al., 2019), which were determined by trial and error to match the mechanical behaviour of sands in triaxial compression tests. For the parameters of MH bond part, the MH strength and stiffness can be calculated by Equations (23) and (17) at a given THC condition. The values for bond parameters *mcri* (i.e. critical slenderness ratio of hydrate) and νb come from (Shen and Jiang, 2016; Jiang et al., 2019), where a detailed discussion was given on their physical meaning. In this work the numerical MHBS specimens were always generated in a loose state at a void ratio $e_0 = 1.0$ with a MH saturation of $S_{MH} = 40\%$, which leads to a hydrate radius multiplier $\lambda = 0.9$.

Table 3 Parameters of MHBS contact model used in DEM analyses

	Parameter of model	Numerical value
Particle part	Particle modulus E_p (N/m^2)	7×10^8
	Particle normal tangential stiffness ratio ξ	5.0
	Particle anti-rotation coefficient β	0.25
	Particle local crushing coefficient ζc	4.0
	Coefficient of particle friction μ	0.5
MH bond part	Elastic modulus of hydrate E_b (N/m^2)	Estimated from T-H-C conditions
	Tensile strength of hydrate σ_t (N/m^2)	
	Compressive strength of hydrate σ_c (N/m^2)	

	Hydrate radius multiplier λ	Estimated from MH saturation
	Critical slenderness ratio of hydrate m_{cri}	0.05
	Hydrate poisson ratio v_b	0.32

3.1 Calibration of MH bond strength accounting for size effect

The size of hydrate bonds in MHBS is much smaller than the size of pure hydrate specimens employed in the laboratory tests that led to Equation (16). Many experimental results show that the quasi-brittle materials, like ice (Jones and Chew, 1983), concrete (Carpinteri et al1999), as well as soils (Garga, 1988) exhibit a dependence of the nominal stress at the ultimate load on the specimen size. In general, the strength of large soil or ice specimen is less than that of small samples that are free from major discontinuities. In addition, Wang et al. (Wang et al., 2020) have found that tensile and compressive failures of MH exhibit an obvious size effect under a certain condition, and the maximum stress decreased with an increase in the size of MH. Consequently, as a brittle material, the size effects of MH are expected to make the bond strength in MHBS higher than that of the conventional MH specimens in laboratory.

Volume size effects on the strength of brittle materials are usually described by a Weibull approach (Weibull, 1939). In the Weibull theory, the volume dependence of the strength of brittle materials is given by Petrovic (1987):

$$(\sigma_2/\sigma_1) = (v_1/v_2)^{1/m} \tag{24}$$

where σ is the applied tensile stress which is assumed to be uniform over the stressed volume of material, v is the stressed volume, and m the Weibull modulus. Weibull

volumetric scaling is often applied in DEM simulations dealing with particle fragmentation (e.g. (Ciantia et al., 2015). To evaluate the magnitude of likely size effects, in this case a cylinder of 50 mm in diameter and 75 mm in height, such as those employed in (Li et al., 2012), was used as reference volume $v1$ to evaluate strength ratio for the bond volume that was later used in the simulations. Ice is generally recognized as a good analogue for MH and has a Weibull modulus of approximately 5, according to (Petrovic, 2003). The ratio of bond strength to specimen strength is represented in Fig. 12 for a range of Weibull modulus close to that of ice. The results indicate a potentially large size effect.

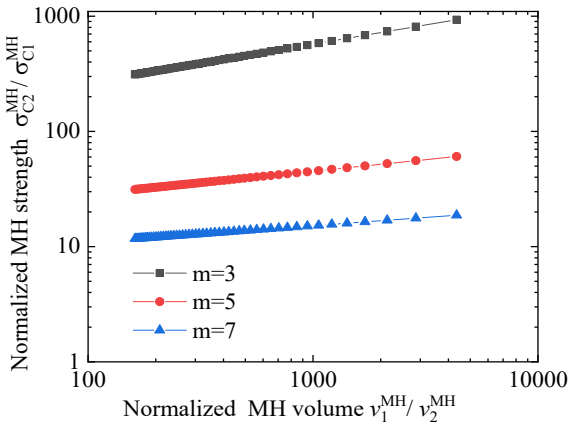

Fig. 12 Normalised MH strength as a function of methane hydrate volume

To calibrate the size-effect correction coefficient αs more precisely, a series of conventional triaxial compression tests were simulated on MH bonded glass beads (Kajiyama et al., 2017) with different αs (i.e. α_s = 10, 20, 30, 40, 50) to adjust the value of αs. The simulations were performed on a prismatic specimen with a size of 3.4 mm × 3.4 mm × 6.8 mm, containing about 10,000 particles. Fig. 13 presents the numerical results for a value of αs = 30, which demonstrates that the DEM results agree well with

the experimental data in (Kajiyama et al., 2017). Such agreement proves that $\alpha_s = 30$ is a reasonable value that further leads Fig. 12 to suggest that the Weibull modulus *mw* for MH is about 6, which seems reasonably close to the value quoted for ice. To our knowledge, this is the first time a Weibull modulus for methane hydrate has ever been put forward. In Fig. 13, the deviatoric stress is defined as $q=\sqrt{1/2[(\sigma_1'-\sigma_2')^2+(\sigma_2'-\sigma_3')^2+(\sigma_1'-\sigma_3')^2]}$, where σ_1', σ_2' and σ_3' are the major, intermediate, and minor effective principal stress, respectively. The slight difference in Fig. 13 was attributed to the fact that a part of the hydrate may be available in pore space of the sample in experiment to connect the rounded grains, which made the movement of grains a difficult task. In addition, a small amount of MH may be available on the surface of beads, forming irregular shape, even after MH cementation breaks. These in return resulted in the rapid increment of bulk modulus for methane hydrate-bearing glass beads. However, in our DEM simulations, as described in Section 2 and our previous studies, MH is assumed to exist solely at contacts between particle to cement particles and the contact model incorporating rolling and twisting resistances was used, in which a shape parameter β was introduced, to capture the effect of real particle shape.

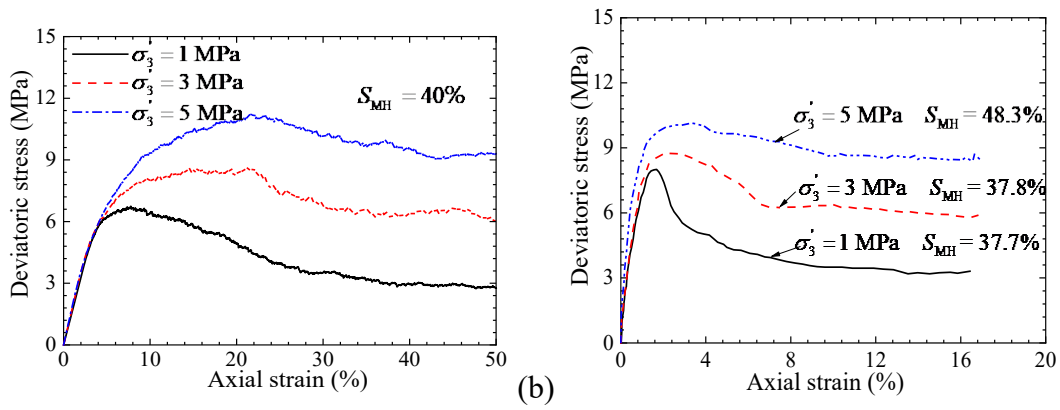

(b)

Fig. 13 Shear stress against axial strain: (a) DEM results, (b) experimental results [62]

3.2 Validation of THMC contact model of MHBS

We shall now validate the THMC contact model. Fig. 14 presents the stress–strain -volumetric responses of MHBS sample obtained from the conventional triaxial compression DEM simulations and experiments (Hyodo et al., 2013). It can be observed that increase of temperature or decrease of initial back pressure leads to low shear strength and less dilatancy in both the DEM simulations and experiments. In addition, samples with different temperature or different pressure have different initial void ratio before shearing. These phenomena are reasonable. According to the work in Section 2, high (low) temperature or low (high) pressure condition will lead the temperature–pressure dependent parameter L to a small (large) value, resulting in a weak (strong) cementation strength at contacts between pairs of MHBS particles, which will further give rise to a small (large) strength, dilatancy as well as structural yield stress (to be explained in Section 4.1.1) of MHBS. Given a confining pressure, the sample with a small structural yield stress will have large deformation and obvious reduction of void ratio, while the sample of large yield stress will experience small deformation and slight decrease of void ratio. Consequently, after consolidation, samples with different temperature or different pressure have different void ratio before shearing as shown in Fig. 14.

Fig. 15 illustrates the effect of ambient temperature and pressure on the peak strength $q_{\max}$ and secant modulus E_{50} of MHBS in the DEM simulations and experiments (Hyodo et al., 2013). The data in the figure are normalized by those of the

host sand for clarity. Fig. 15 shows that despite the slight differences between the numerical and experimental results caused by the simplifications in particle shape and contact model, the high temperature or low initial back pressure leads to low normalized peak strength q_{max} and secant modulus E_{50} in both the DEM simulations and experiments. Overall, the MHBS behavior obtained numerically is in qualitative agreement with that observed experimentally. Figs 14 and 15 demonstrate that the DEM incorporating the proposed THMC model is able to capture the main behaviour of MHBS under different temperature, initial back pressure (pore water pressure) conditions. Note that in the current study, the void ratio refers to the granular void ratio which treats the hydrate volume as part of the pore volume. The role of cement is assumed to be identical before and after bond breakage in affecting the volumetric behaviour with regard to bond fragments. When there is no cement/bond failure, the MHBS can be regarded as anelasticity. According to the theoretical formula in Table 2 and in Jiang and Zhu (2007), the cementation content will change the values of normal stiffness kn and tangential stiffness ks between a pair of spherical particles, as well as the macroscopic modulus E and Poisson ratio vp of the bonded assembly. When there is cement failure, the dilatancy as well as Eb 50 of the bond assembly will be reduced slightly in the DEM analyses due to the assumption that there is no fragmented cement filling in the pores, but this effect is quite limited. This is due to the fact that under a given load, a considerable amount of bonds are not damaged even within the shear band of the sample at large strain. bonds form cemented clusters, which greatly increases the dilatancy of the assembly (Jiang et al., 2011). Compared to this effect, the effect of the

bond fragments can be neglected on its dilatancy/E^b_{50}. We shall examine if the DEM can capture the effect of salinity in the next section.

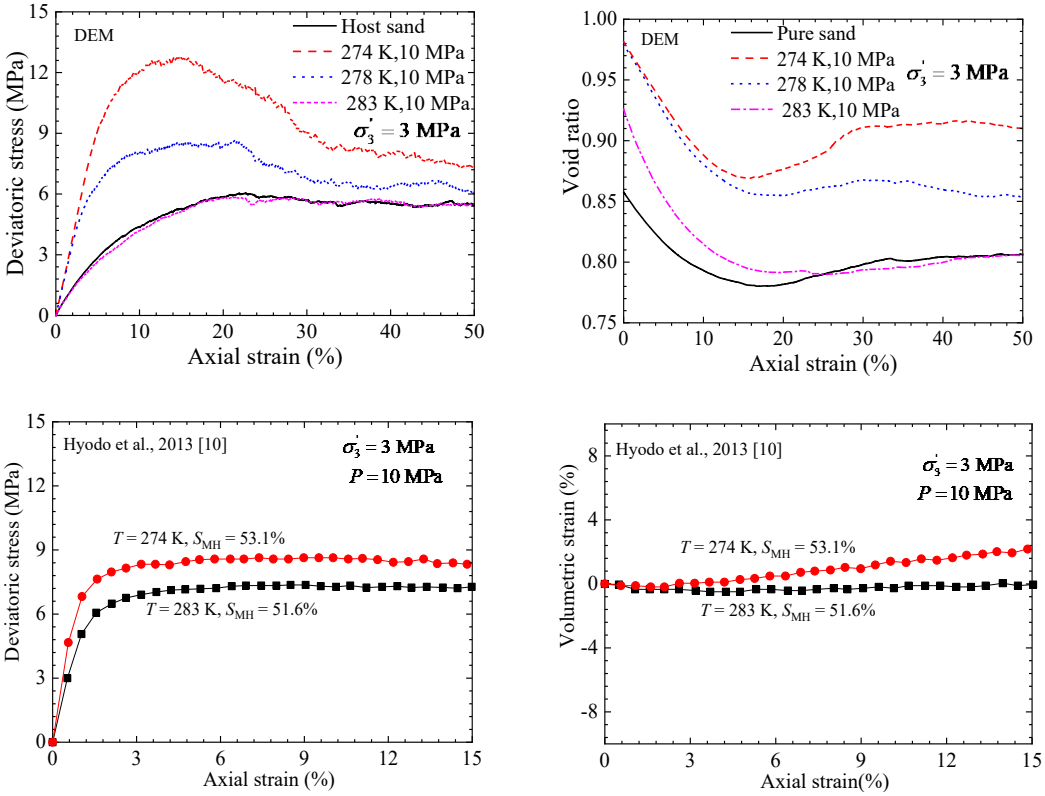

(a)

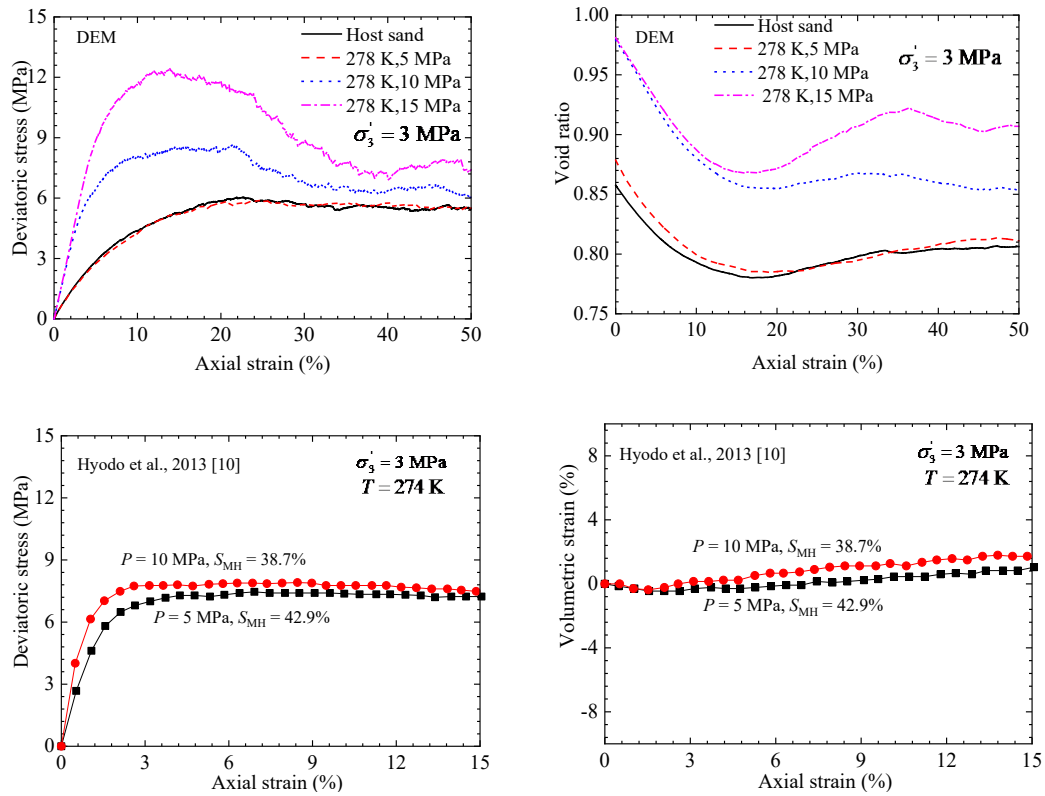

(b)

Fig. 14 Stress strain and volumetric responses of MHBS from DEM simulations and experiments:(a) different temperature, (b) different initial back pressure

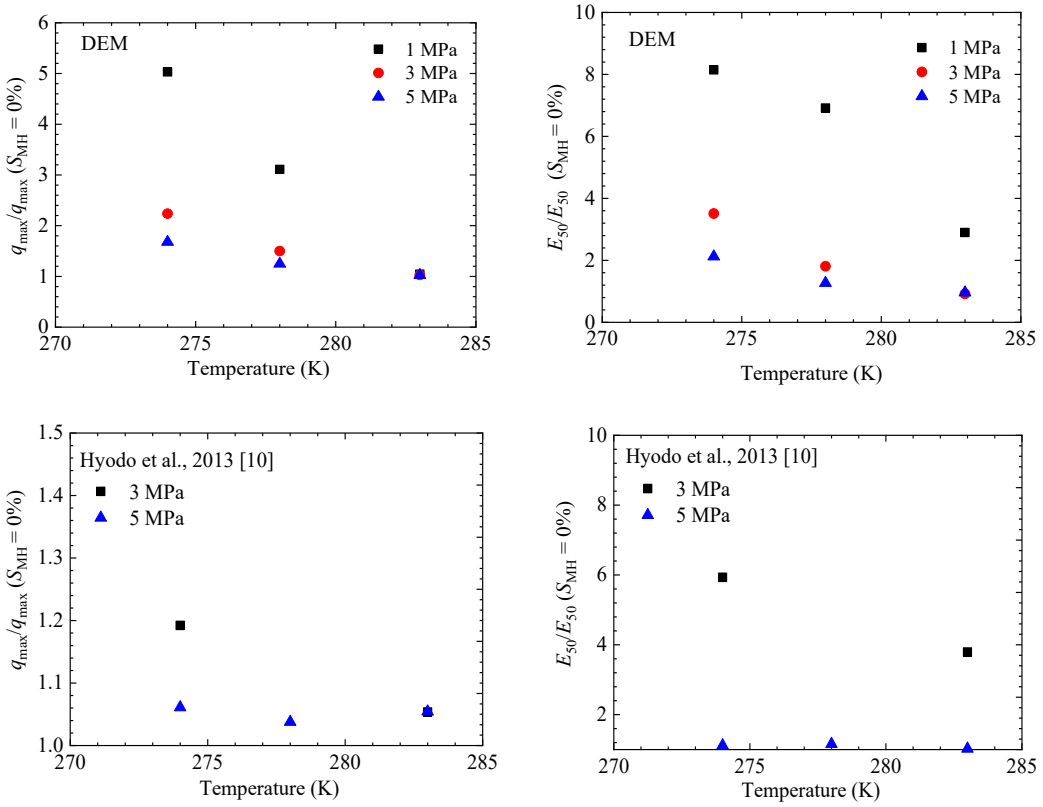

(a)

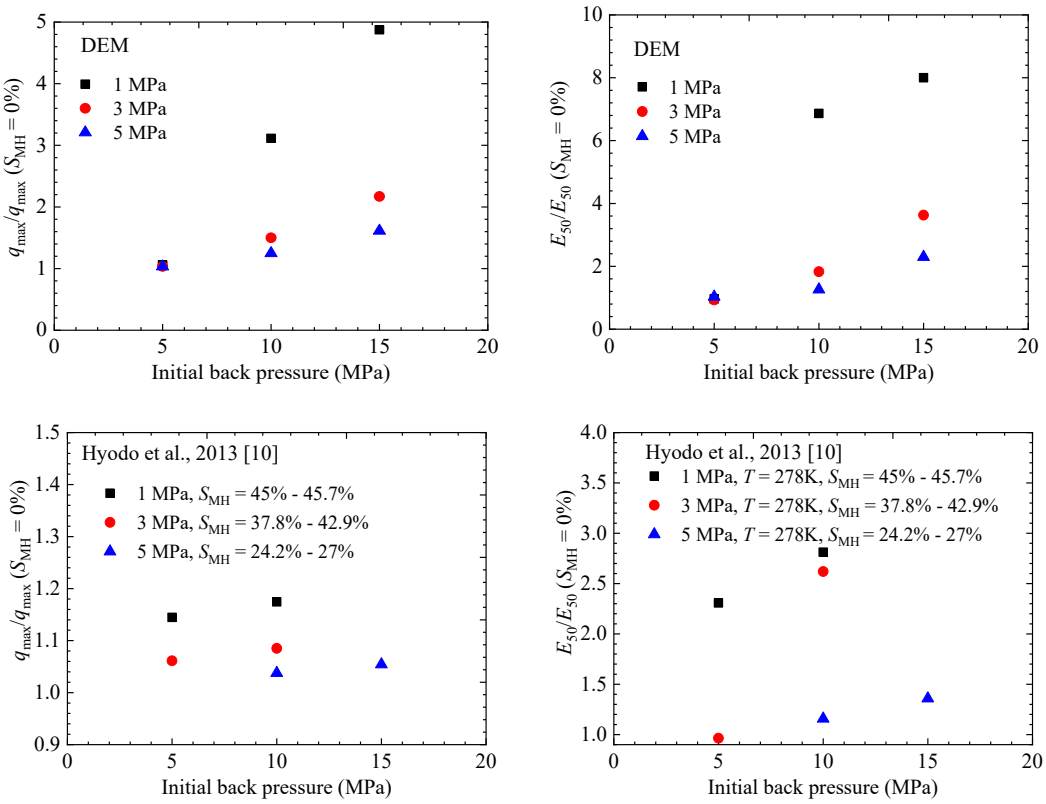

(b)

Fig. 15 Peak strength q_{max} and secant modulus E_{50} responses of MHBS from DEM simulations and experiments:(a) different temperature, (b) different initial back pressure

4. Salinity effects on MHBS response along various stress paths

In this section, isotropic compression (IC), conventional triaxial compression (CTC) and constant stress ratio (CSR) tests are numerically simulated by the DEM. The results are presented using the mean stress $p'=(\sigma_1'+\sigma_2'+\sigma_3')/3$ and the deviatoric stress q.

Fig. 16 illustrates the configuration of the DEM sample and the stress paths in the IC, CTC and CSR tests. Prismatic samples with a size of 5.5mm×5.5mm×11mm are used in CTC tests, while a cubic specimen with a side length of 6.8mm is employed in IC and CSR tests. Each sample has about 40000 particles, and is confined by six frictionless boundary walls. First, the sample is one-dimensionally compressed under a vertical stress of 200kPa until it arrives at the equilibrium state, after which different loading path is employed for performing different test as shown in Fig. 16(c). In the IC test, the sample is gradually and isotropically compressed to 40MPa in the way of $\sigma_1'=\sigma_2'=\sigma_3'$. In the CTC test, the sample is first isotropically compressed to a confining pressure, e.g., 1MPa, 3MPa, 5MPa respectively, and then sheared by moving the top and bottom walls with a constant velocity until the axial strain reaches 50% while the confining pressure remains constant. In the CSR test, the vertical stress σ_1' is gradually increased by moving the top and bottom walls, and the horizontal pressure ($\sigma_2'=\sigma_3'$) is controlled by a servo-mechanism to keep stress ratio $\eta_{CSR}=\sigma_3'/\sigma_1'$ a constant, until the

mean stress reaches 40MPa or the axial strain arrives at 30%.

All the DEM tests were performed at four different value of salinity, i.e., 0 wt%, 3 wt%, 6 wt%, and 10 wt% respectively, while the temperature and water pressure condition remains 278K and 10MPa.

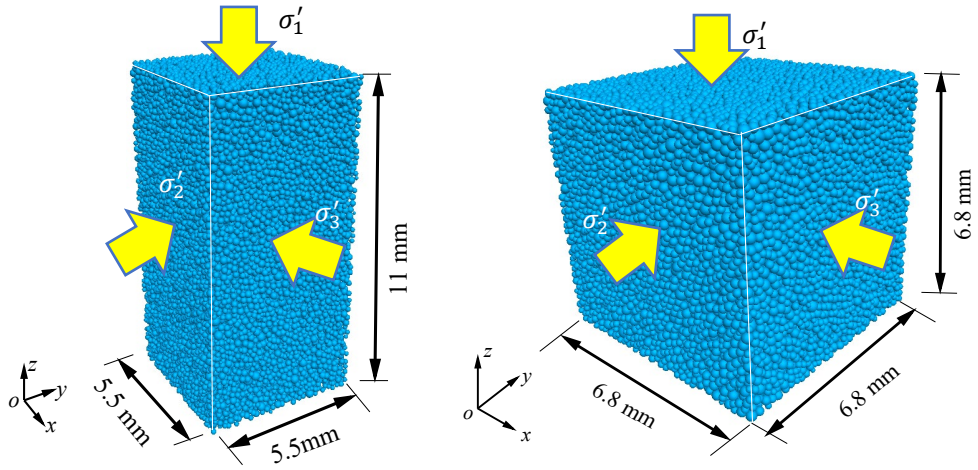

(a) Prismatic sample (b) Cubic sample

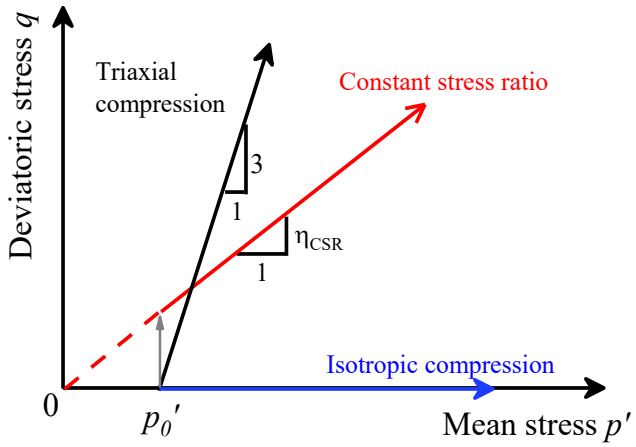

(c) Stress paths

Fig. 16 Configuration of the DEM samples and the stress paths used in the simulations

4.1 Effect of salinity on MHBS in the isotropic compression tests

4.1.1 Relationship between yield and bond breakage

Fig. 17 presents the void ratio and bond breakage ratios of specimens with different value of salinity. The bond breakage ratio is defined as the total number of failed bonds

to the initial bond number. In addition, the bond breakage ratio due to different failure type, e.g., tensile failure or compression failure, is also provided for further analyses.

Note that there are two kinds of yield stresses in geomechanics. The first one is called starting-yield stress which can be defined as the stress condition starting to lead to the bond breakage on microscopical scale (Jiang et al., 2006); and is illustrated by dot in the amplified window in Fig. 17(b). This microscopically-defined starting-yield stress is similar to the starting-yield stress widely used in the geotechnical engineering, e.g. (Rotta et al., 2003), which is defined as the initiation of plastic (irrecoverable) deformation on macroscopical scale. And according to our previous investigation (Jiang et al., 2006), our microscopically-defined starting-yield has the same value as the macroscopically-defined one, which will not be discussed here. The second one is named as structural-yield stress, which can be defined as the stress corresponding to the largest gradient point of the bond breakage ratio curve on microscopical scale (Jiang et al., 2006), and is illustrated by arrow in Fig. 17(b). Also, this microscopically-defined structural-yield stress is quantitatively closed to that used in geotechnical community (Jiang et al., 2006), which is defined as the largest gradient point on the e-p curve as indicated by arrow mark in Fig. 17(a). In this paper, we shall focus on the structural-yield stress. By comparing Fig. 17(a) with Fig. 17(b), it is found that the macroscopic (microscopic) structural-yield stress at 0 wt %, 3 wt%, 6 wt%, and 10 wt% is 8.39 (8.30) MPa, 7.30 (7.20) MPa, 4.46 (4.37) MPa and 2.30 (2.30) MPa, respectively, which demonstrates that the microscopically-defined structural-stress is nearly identical to the macroscopically-defined one on the compression curve in value. In addition, the higher

the environmental salinity is, the more obvious the structural-yield point, the higher the bond breakage ratio and the smaller the corresponding yield stress become.

Salinity effects are particularly visible in the rate of bond destruction, which is quite fast in the relatively high saline cases. This is because the mechanical properties of MH are closely related to the salinity condition as well as others. MH is a kind of temperature–pressure-salinity-sensitive material. As shown in Fig. 9, as the NaCl concentration increases, the MH phase equilibrium line shifts gradually to the right side on the normalized temperature–pressure scale, which will lead to the fact that in any given condition on pressure and temperature, different value of NaCl concentration makes the MH have different value of L, as mentioned previously. In the process of the transition of the temperature–pressure-chemical point from low salinity concentration to high salinity concentration, MH bond deteriorates and becomes damaged under a given load, which in turn results in the reduction of the yield stress, strength and stiffness of MHBS. This phenomenon can be linked with the basic equations proposed in the micro constitutive model. Equations (21) and (22) show that parameter L decreases with the increase of salinity w, while Equations (17) and (23) demonstrate the secant modulus $E50$, compression strength σc and tension strength σt of the MH bond decrease with decreasing of L. Consequently, $E50$, σc and σt of the MH bond decrease with the increase of w. Therefore, if the salinity level is high, the MH bond will break fast, resulting in a quick increase in bond breakage ratio. Although there is no direct experimental data on MHBS to verify the above conclusions, there are many other experimental data on the influence of chemical condition/cement content on

cemented sand (Qabany and Soga, 2013; Liu et al., 2019; Wang and Leung, 2008), which demonstrates that the bonding effect varies at different chemical condition/cement content. This is because different chemical condition/cement content leads to different strength and stiffness of cementation between particles, which further affects the mechanical behaviour of cemented sands. In addition, Fig. 17 shows that hydrate bond breakage is mainly caused by compression failure, while there are a few tensile failure. At the high pressure, all the compression curves converge, as mechanical debonding is almost complete and the MHBS behaves mostly like the pure sand.

.

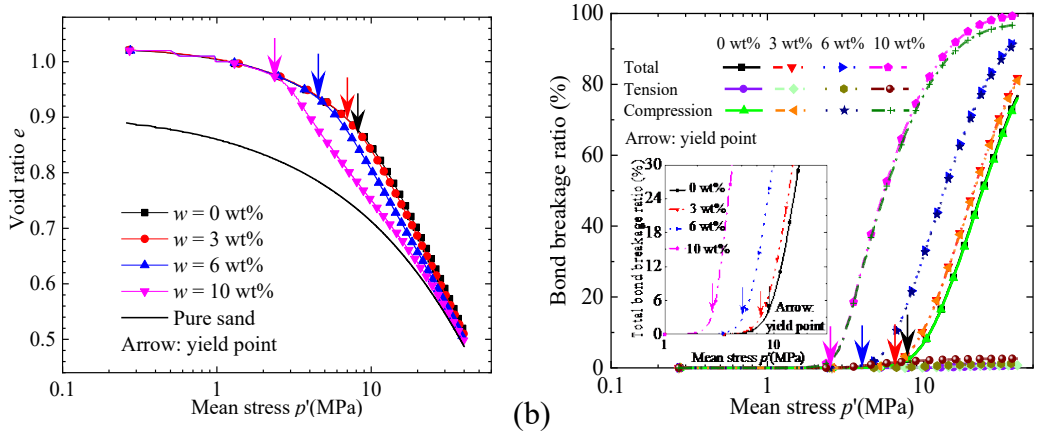

Fig. 17 Effect of salinity on the isotropic compression responses of the MHBS: (a) compression curves, (b) bond breakage ratios

4.1.2 Mechanical coordination numbers and stress components

Fig. 18 (a) presents the variation of mechanical coordination numbers obtained from the DEM isotropic compression test on MHBS under different salinity. The mechanical coordination number is defined as $Z_m=(2N_c-N_{p1})/(N_p-N_{p1}-N_{p0})$ [86], where N_c is the number of contacts, N_p the total number of particles. N_{p1} and N_{p0} are the number

of particles with only one or no contacts respectively. It is recognized that in DEM simulations the mechanical coordination number has a closer relation with macroscopic quantities such as stress and porosity than the conventional coordination number $Z=2N_c/N_p$.

Fig. 18 (a) shows that the mechanical coordination number Z_m for the MHBS remains nearly constant before the initial yielding. After the initial yielding where a large number of bonds break, the total coordination number begins to increase, while the mechanical coordination number restricted to bonded contacts Z_m^b decreases. With the increase of salinity, the reduction rate of bond mechanical coordination number increases.

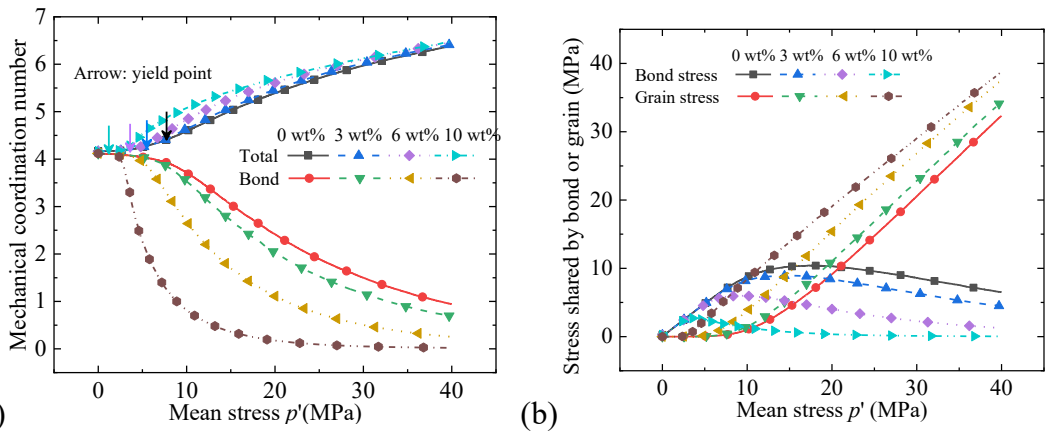

Fig. 18 Effect of salinity on the isotropic compression responses of MHBS: (a) mechanical coordination numbers, (b) stress components

In the MHBS specimen the force between the soil particles is shared by the hydrate cement part and the non-cement part. Nominal stresses in discrete element analyses may be computed by (Christoffersen et al., 1981):

$$\bar{\sigma} = -\frac{1}{V}\sum_{N_c} F^{(c)} \otimes L^{(c)} \tag{25}$$

where $\bar{\sigma}$ is the stress in the element, $\boldsymbol{F}^{(c)}$ is the contact force, $\boldsymbol{L}^{(c)}$ is the contact direction

vector, V is the total volume of the element. A bond stress component is obtained if the formula is applied by using only forces due to the bond contact part. Similarly, if only forces due to uncemented particle contact are used, grain stress component is obtained.

Fig. 18 (b) provides the stress component evolution measured in the DEM isotropic compression tests on MHBS under different salinity. Fig. 18 (b) shows that the general evolution trend is similar in all the cases. At the beginning, total force is transmitted by the hydrate cementation and the grain stress component is almost null. As the mean stress increases, the bond stress component gradually increases until the bond breakage appears, after which the bond stress component decreases and the grain stress one increases. Increased salinity accelerates this process, reducing the peak bond stress component achieved at lower mean stress.

4.2 Effect of salinity on MHBS in the triaxial compression tests

4.2.1 Macroscopic behaviour

Fig. 19 (a) shows the stress-strain relationships obtained from the DEM triaxial compression test at 3MPa confining stress on pure sand and cemented MHBS with different salinity. It can be observed that the cemented MHBS exhibits obvious strain-softening characteristics which is stronger at a lower environmental salinity w. Peak shear strength measured from MHBS is smaller at high salinity than at low salinity. Note that when the sample reaches its residual strength, the bond breakage ratio is relatively high, resulting in a small difference on residual strengths in Fig. 19(a). Moreover, as the NaCl salinity increases, the relationship obtained from MHBS appears close to that of the pure sand.

Fig. 19 (b) presents the peak and residual stresses for the DEM MHBS specimens with different salinity and confining stress. It shows that the peak (residual) stress of MHBS decreases by 0.3 (0.06) MPa with an increase of 1wt% in salinity. In addition, the higher the confining stress is, the higher the peak and residual stresses are.

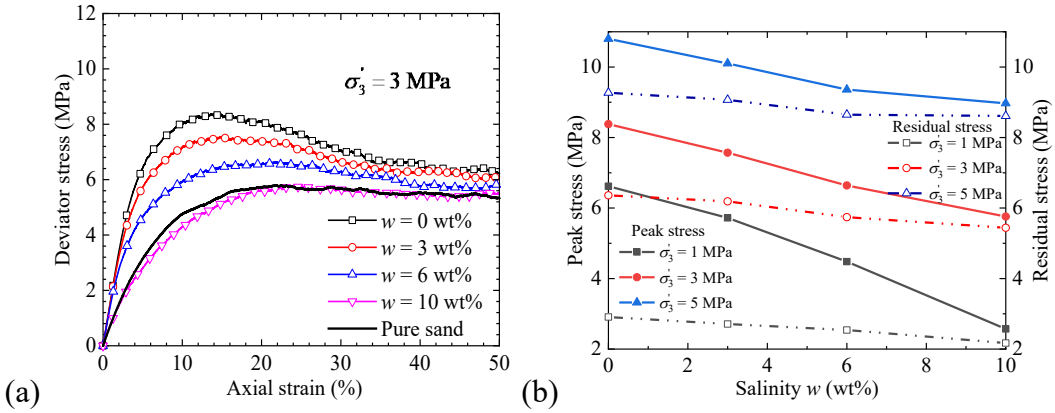

Fig. 19 Stress-strain relationships and stresses from the DEM conventional triaxial tests on MHBS and pure sand with different salinity and confining stress: (a) stress-strain relationships, (b) peak and residual stresses

Fig. 20 provides the void ratio measured in the DEM triaxial test on MHBS and pure sand with different salinity and confining stress. Fig. 20 (a) shows that the MHBS specimens demonstrate a predominantly contractive response at $\sigma'3$ = 3MPa, and the contraction increases with the increase of salinity, while Fig. 20 (b) demonstrates that such contraction increases with the increase of confining stress. Again, it should be noted that when confining pressure or salinity is higher, the MHBS sample will be compressed more obviously during the process of isotropic consolidation, resulting in that the void ratio of sample is smaller than others at the beginning of shearing. In contrast, Fig. 20 (c) shows that, in general, the higher the confining pressure, the smaller the final void ratio of MHBS sample. In addition, the salinity effect is more obvious under lower confining stress. This is because when confining stress is smaller than the

yield stress of MHBS sample, the sample retains its intact structure with large void ratio. As a result, the final void ratio of MHBS after shearing in Fig. 20 (c) decreases more quickly with the increase of salinity under lower confining stress.

Fig. 21 illustrates the effect of ambient salinity on the peak strength q_{max} and secant modulus E_{50} of MHBS measured in the DEM triaxial tests. Note that the data are normalized by those of the host sand in the figure. Fig. 21 shows that the increase in salinity will reduce the normalized peak strength and secant modulus, particularly at low confining stress.

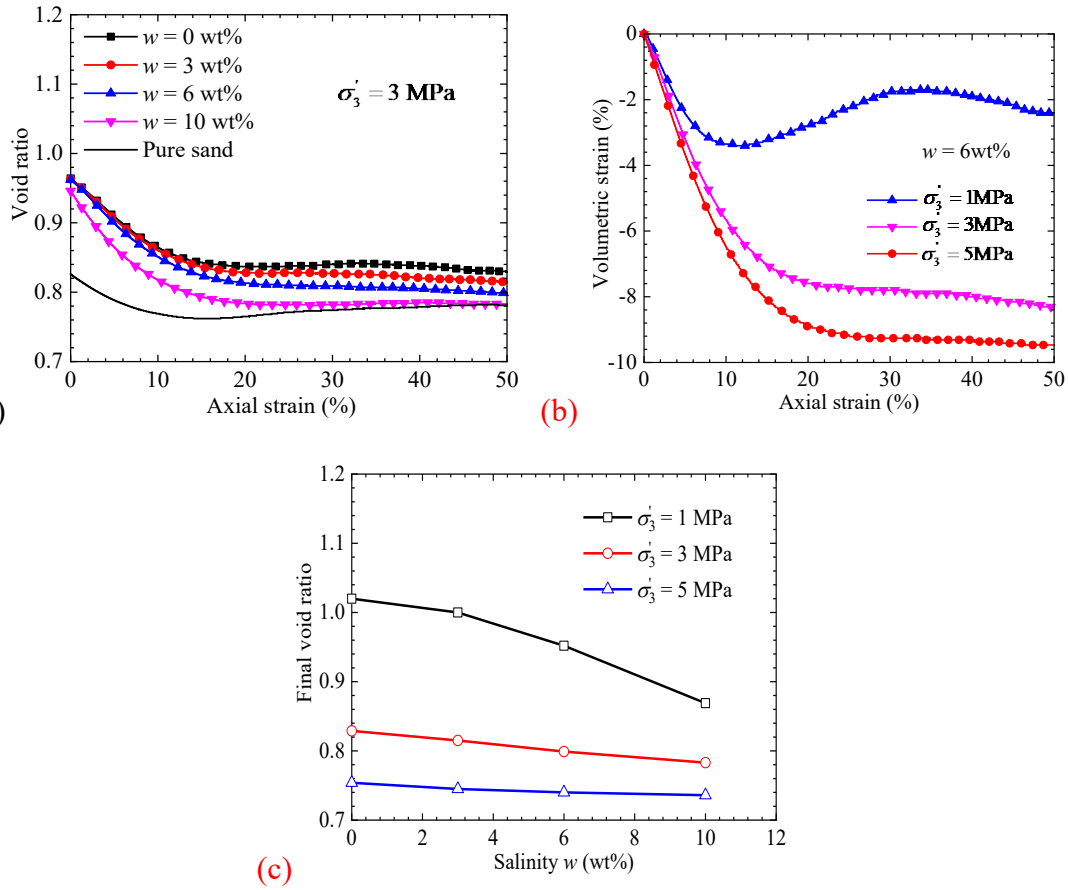

Fig. 20 Void ratio and volumetric strain measured in the DEM triaxial test on cemented MHBS with different salinity and confining stress: (a) variation of void ratio, (b) variation of volumetric strain, and (c) final void ratio

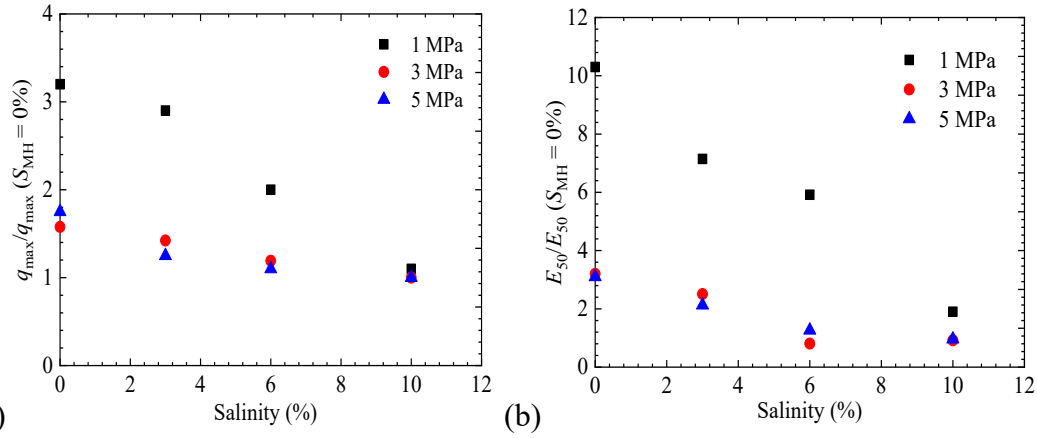

Fig. 21 Peak strength q_{max} and secant modulus E_{50} responses of MHBS from the DEM simulations at different salinity: (a) normalized peak strength, (b) normalized secant modulus

4.2.2 Microscopic behaviour

Fig. 22 presents the evolution of bond breakage ratios, mechanical coordination numbers and stress components measured in the DEM triaxial compression tests on MHBS under different salinity and confining pressure. Fig. 22 (a) shows that the bond breakage ratios increase with the increasing of axial strain and salinity. Bond breaks mainly in a compression failure mode, and there is also a fraction of bonds that fail in a tensile mode. The reason why the effect of salinity is weak under large confining stress appears clear in Fig. 22 (b): the shear under large confining stress is able to break the majority of the bonds which therefore diminishes the impact of salinity.

Fig. 22 (c, e) show that the total mechanical coordination number and grain stress component increase quickly at first and then gradually to a constant with the increasing of axial strain, while the bonded mechanical coordination number decreases fast at first and then slowly toward its residual one. In contrast, the bond stress component firstly increases to a peak value and then decreases towards a constant. Fig. 22 (d, f) show that

at the end of the tests, where most of the debonding has already occured, the salinity demonstrates obvious (slight) effect on bonded (total) coordination number and bond (grain) stress component. However, with the increase of confining stress, the total (bonded) mechanical coordination number and grain (bond) stress component increase (decrease).

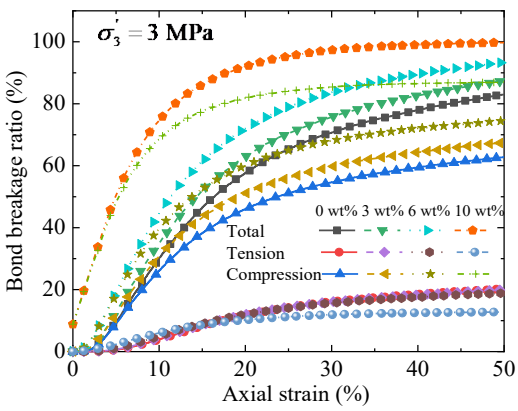

(a) Bond breakage ratios

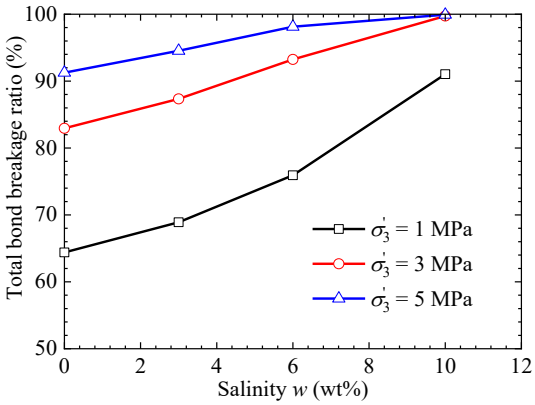

(b) Total bond breakage ratio at the end of test against salinity

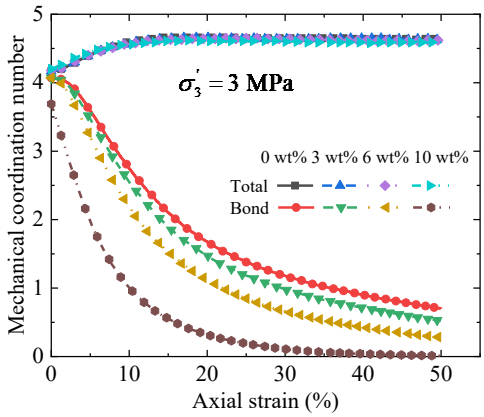

(c) Mechanical coordination numbers

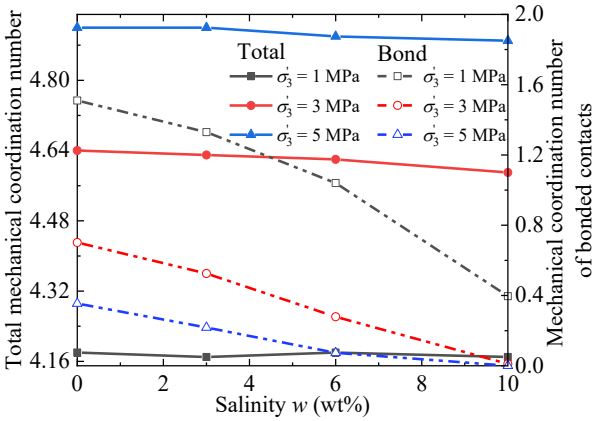

(d) Mechanical coordination numbers at the end of test against salinity

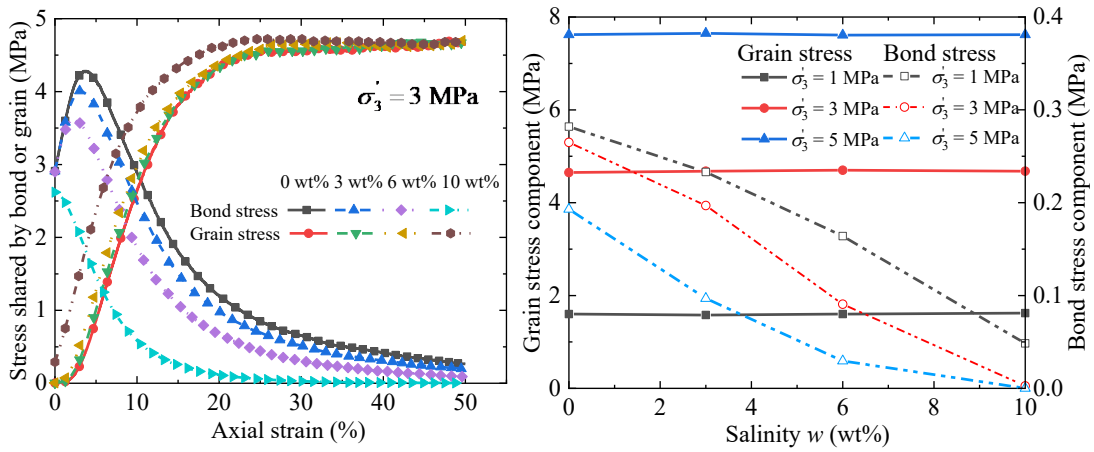

(e) Stress components

(f) Grain stress and bond stress at the end of test against salinity

Fig. 22 Mechanical responses of MHBS specimens obtained from the DEM triaxial compression tests

4.3 Effect of salinity on MHBS in the constant stress ratio tests

In the CSR tests, as illustrated in Fig. 16(c), the DEM specimens are initially compressed isotropically to the target mean effective stress of p_0' and then loaded at a desired stress ratio $\eta_{CSR} = \sigma_3'/\sigma_1'$, η_{CSR} = 0.3, 0.6 and 0.9 respectively, in the study.

4.3.1 Macroscopic behaviour

Fig. 23 (a, b) presents the compression curves obtained from the DEM CSR tests on MHBS samples under different constant stress ratio at w = 3 wt% and w = 10 wt%, respectively. The compression curve for the pure sand is provided for comparison in the figure as well. Here the yield point represents the structural-yield again, corresponding to the largest gradient point on the e-p curve on macroscopical scale as we mentioned before, and is illustrated in Fig. 23(a) and (b) by the arrow marks. Fig. 23 (c) presents the stress–strain relationships of the DEM MHBS samples with different salinity but at a stress ratio of 0.3. It shows that both the peak and residual deviatoric stresses decrease obviously with the increase of salinity, like Fig. 19 observed in CTC

tests. Fig. 23 (d) provides the evolution of final void ratio and macroscopical structural-yield stress with different salinity at the mean stress of 40 MPa. Hence, only the final void ratios measured at the stress ratio of 0.6 and 0.9 are provided in the figure. Fig. 23(d) shows that the higher the environmental salinity is, the smaller the final void ratio in all the cases and the lower the macroscopical structural-yield stress becomes.

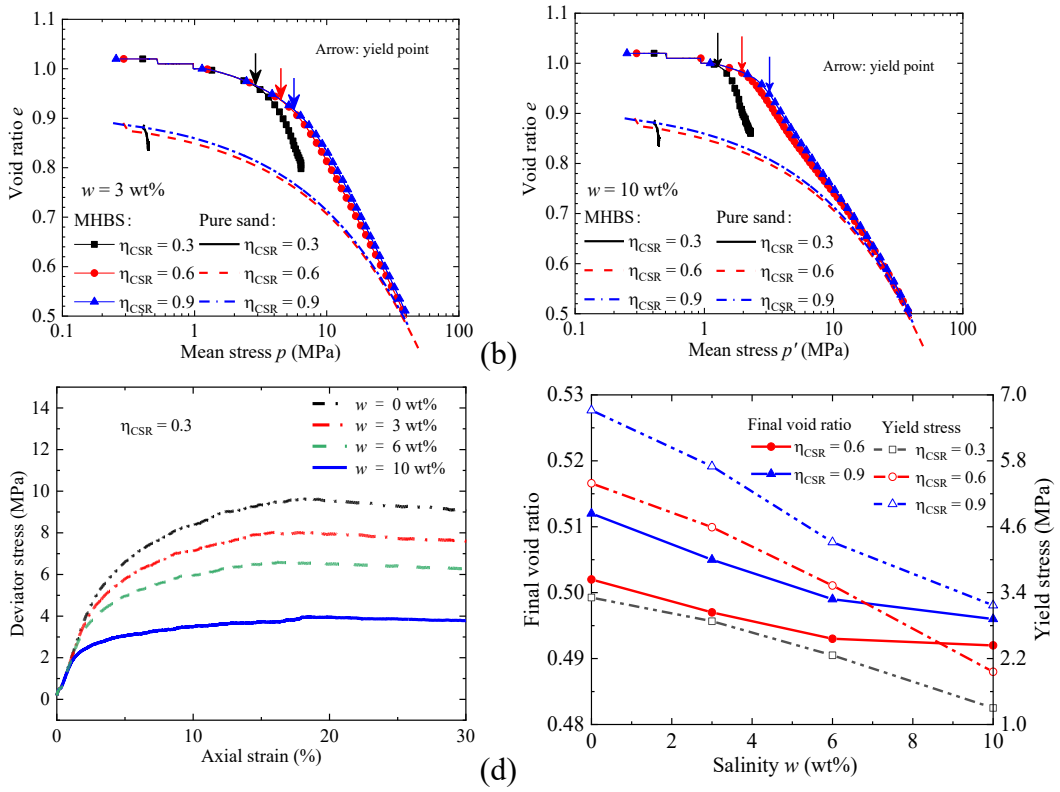

Fig. 23 Effect of salinity on the responses measured in DEM constant stress ratio tests on MHBS: (a-b) compression curves, (c) stress-strain relationships, (d) final void ratio and yield stress

4.3.2 Microscopic behaviour

Fig. 24 presents the evolutions of bond breakage ratios, mechanical coordination numbers and stress components obtained from the DEM CSR tests on MHBS under different salinity and constant stress ratio. Fig. 24(a) shows that the bond breakage ratios of MHBS gradually increase with the increase of mean stress, and the bond

breakage is mainly due to bond compression failure, regardless of salinity. However, under a higher salinity environment, the increasing rate of the bond breakage increases faster to a higher peak value, e.g. the bond breakage ratio reaches almost 100% at a mean stress of 40MPa under a salinity of 10wt%, while it only reaches 80% under a salinity of 3wt%. Fig. 24(b) summarizes the bond breakage ratio and microscopic structural-yield stress against salinity at the end of test. Again, the microscopic structural-yield stress is the stress corresponding to the largest gradient point on the bond breakage ratio curve, and is illustrated by arrow in Fig. 24(a) and clarified in the amplified window. Fig. 24(b) shows that at the end of the tests, the bond breakage ratio increases while the microscopic structural-yield stress decreases with the increase of salinity. In addition, comparison between Fig. 23(d) and Fig. 24(b) shows that when ηCSR = 0.3/0.6/0.9, the macroscopic (microscopic) structural-yield stress at 0 wt%, 3 wt%, 6 wt%, and 10 wt% is 3.31/5.39/ 6.72 (3.27/5.35/6.64) MPa, 2.88/4.59/5.7 (2.8/4.53/5.59) MPa, 2.26/ 3.53/4.32 (2.18/3.48/4.27) MPa and 1.3/1.96/3.17 (1.19/1.88/3.11) MPa, respectively, which demonstrates again that the microscopically-defined structural-yield stress has a value close to the macroscopically-defined one. With regard to the mechanical coordination numbers shown in Fig. 24(c, d), it can be observed that with the increase of the mean stress, the bonded mechanical coordination number decreases quickly at first and then gradually to a constant in a way associate with salinity, while the total mechanical coordination number increases gradually regardless of salinity. In contrast, with the increase of salinity, the bonded (total) mechanical coordination number decreases (increases), as shown in Fig. 24(d). In terms

of the stress components shown in Fig. 24(e, f), it is shown that the stress shared by bond increases to a peak value at first and then decreases to a constant, while the stress shared by grain increases gradually, in a way associated with the salinity. The bond (grain) stress component decreases (increases) with the increasing of salinity. Such observations are similar to those in triaxial compression tests shown in Fig. 22(e, f). Moreover, Fig. 24(b, d, f) show that at the end of tests, with the increase of stress ratio, the bond breakage ratio (micro-structural-yield stress), total (bonded) mechanical coordination number and grain (bond) stress component decrease (increase).

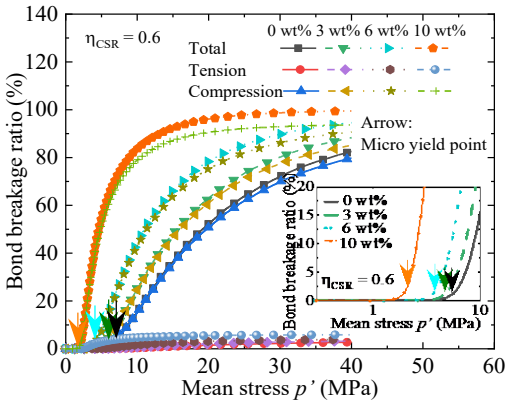

(a) Bond breakage ratios

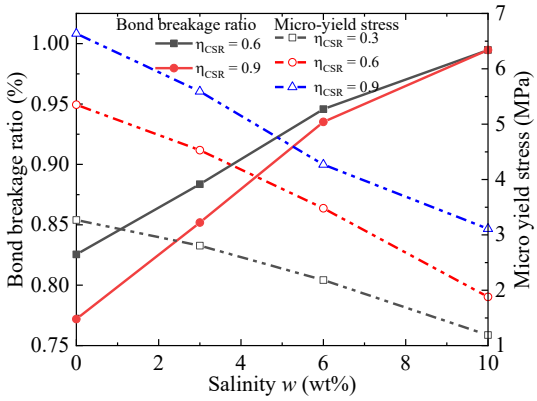

(b) Total bond breakage ratio and microscopic yield stress at the end of test against salinity

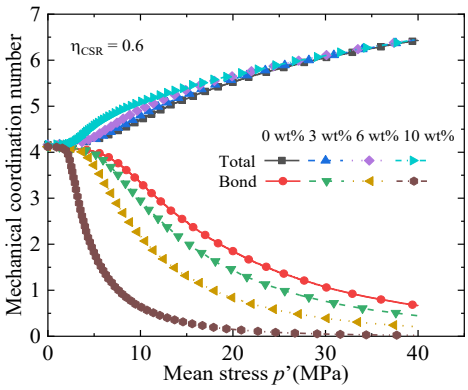

(c) Mechanical coordination numbers

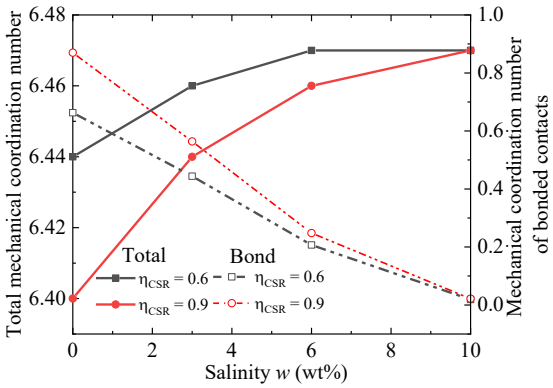

(d) Mechanical coordination numbers at the end of test against salinity

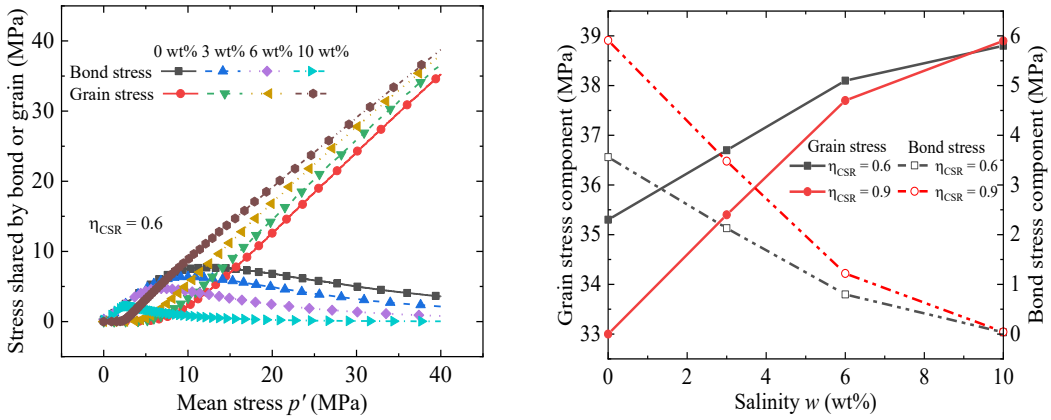

(e) Stress components

(f) Grain stress and bond stress at the end of test against salinity

Fig. 24 Mechanical responses of MHBS specimens obtained from the DEM constant stress ratio tests

5. Conclusions

This study presents a DEM study on the macroscopic and microscopic mechanical behaviour of methane hydrate bearing sediments (MHBS) at different salinity in isotropic compression, conventional triaxial compression and constant stress ratio tests to develop constitutive models for MHBS and have safe exploitation of MH resources in the future. A novel three-dimensional (3D) thermo-hydro-mechanical-chemical (THMC) contact model for MHBS was proposed, and implemented into a DEM software to simulate the three-type tests for this aim. Focus is on the stress–strain relationships, macro- and micro- structural-yield stresses, strengths, bond breakage ratios, mechanical coordination numbers and stress components of the samples under different salinity in these tests. The main conclusions are as follows::

(1) A simple formulation was proposed to take into account the salinity effect in the contact model for MHBS. Size effects on MH bond strength have been explicitly accounted for in calibration. The DEM simulations with the model captures well

the effect of temperature or initial back pressure (i.e. pore water pressure) on stiffness, shear strength and dilatancy of MHBS observed in experiments (Hyodo et al., 2013).

(2) The peak and residual stresses of MHBS increase with the increasing of confining stress in the DEM simulations. At the end of tests, with the increase of confining stress or decrease of stress ratio, the bond breakage ratio (structural-yield stress), total (bonded) mechanical coordination number and grain (bond) stress component increase (decrease). These observations are reasonable.

(3) Further DEM results indicate that macro- and micro- yield stresses, the shear strength and stiffness of MHBS decrease with the increasing of salinity, which is related to the evolutions of bond breakage, stress components and mechanical coordination numbers. The increase of salinity drives the stress component transit from bond-dominant to grain-dominant leading to increased contraction. During plastic shearing, i.e. post –yield, the total (bonded) mechanical coordination number of MHBS increases (decreases). This transition is accelerated by the increasing of salinity. These are due to the fact that at large salinity, most bonds break quickly and force transmission occurs through uncemented contacts.

It is worth mentioning that the model is proposed resting on the hypothesis that the shifts in stability conditions due to the presence of NaCl would directly affect the strength and modulus of the MH. Such shift law will be assumed to extend to MHBS without any change. Currently, the mechanical behaviour of MHBS under different salinity have not been examined in laboratory tests, which indicates that the model as

well as numerical results in this paper go ahead of and hence need verification from experimental work. Nevertheless, our work is meaningful because the experiments are so difficult and time-consuming to carry out that a well-calibrated model such as that presented in this paper is helpful to develop, not only the techniques, but also the investigation plans for the experiments in the future. In addition, it is also possible to develop the model based on the kinetics of MH dissolution. Because gas hydrate formation and dissociation is a kinetic process of multi-phase and multi-element interaction (Dholabhai et al., 1993; Li et al., 2016). However, such work is beyond the scope of this paper, but will be one of our future works..

Acknowledgement

The work in this paper was financially supported by National Nature Science Foundation of China with Grant Nos. 51890911 and 51639008, and National key Research and Development Program of China with Grant No. 2019YFC0312304, which are sincerely appreciated. In addition, the authors are very thankful to the reviewers for their valuable comments, which have improved the quality of this paper significantly.

References

Booth, J. S., Rowe, M. M., Fischer, K. M., 1996. Offshore gas hydrate sample database: with an overview and preliminary analysis. U.S. Geol. Surv. Open File Rep., 96–272, 31.

Brugada, J., Cheng, Y. P., Soga, K., Santamarina, J. C., 2010. Discrete element

modelling of geomechanical behaviour of methane hydrate soils with pore-filling hydrate distribution. Granul. Matter. 12 (5), 517-525

Carpinteri, A., Ferro, G. A., Monetto, I., 1999. Scale effects in uniaxially compressed concrete specimens. Mag. Concr. Res. 51 (3), 217-225.

Cha, M., Hu, Y., Sum, A. K., 2016. Methane hydrate phase equilibria for systems containing NaCl, KCl, and NH4Cl. Fluid Phase Equilib. 413, 2-9.

Chong, Z. R., Yang, S. H. B., Babu, P., Linga, P., Li, X. S., 2016. Review of natural gas hydrates as an energy resource: Prospects and challenges. Appl. Energy. 162, 1633-1652.

Christoffersen, J., Mehrabadi, M. M., Nemat-Nasser, S., 1981. A micromechanical description of granular material behavior. J. Appl. Mech. 48 (2), 339-344.

Ciantia, M., Arroyo, M., Calvetti, F., Gens Solé, A., 2015. An approach to enhance efficiency of DEM modelling of soils with crushable grains. Géotechnique. 65 (2), 91-110

Cundall, P.A., Strack O.D.L., 1979. A discrete numerical model for granular assemblies. Géotechnique. 29 (1), 47-65.

Dai, S., Santamarina, J. C., Waite, W. F., Kneafsey, T. J., 2012. Hydrate morphology: Physical properties of sands with patchy hydrate saturation. J. Geophys. Res.-Solid Earth. 117, B11205

Dholabhai, P., Englezos, P., Kalogerakis, N., Bishnoi, P., 1991. Equilibrium conditions for methane hydrate formation in aqueous mixed electrolyte solutions. Can. J. Chem. Eng. 69 (3), 800-805.

Garga, V. K., 1988. Effect of sample size on shear strength of basaltic residual soils. Can. Geotech. J. 25 (3), 478-487.

Ghiassian, H., Grozic, J. L., 2013. Strength behavior of methane hydrate bearing sand in undrained triaxial testing. Mar. Pet. Geol. 43, 310-319.

Halliday, W., Clapper, D. K., Smalling, M., 1998. New gas hydrate inhibitors for deepwater drilling fluids. In: Proceedings of the IADC/SPE Drilling Conference, 3-6 Mar, Dallas TX

He, J., Jiang, M.J., Liu, J., 2016. Effect of different temperatures and pore pressures on geomechanical properties of pore-filling type of methane hydrate soils based on the DEM simulations. In: Proceedings of the 7th International Conference on Discrete Element Methods, 827–835.

Huhn, K., Arroyo, M., Cattaneo, A., Clare, M.A., Gràcia, E., Harbitz, C.B., Krastel, S., Kopf, A., Løvholt, F., Rovere, M., Strasser, M., 2019. Modern Submarine Landslide Complexes: A Short Review. Submarine Landslides: Subaqueous Mass Transport Deposits from Outcrops to Seismic Profiles, Geophysical Monograph 246, 181-200.

Hyodo, M., Nakata, Y., Yoshimoto, N., Orense, R., Yoneda, J., 2009. Bonding strength by methane hydrate formed among sand particles. In: AIP Conference Proceedings. 1145 (1), 79-82.

Hyodo, M., Yoneda, J., Yoshimoto, N., Nakata, Y., 2013. Mechanical and dissociation properties of methane hydrate-bearing sand in deep seabed. Soils Found. 53 (2), 299-314.

Hyodo, M., Yoshimoto, N., Kato, A., Yoneda, J., 2013. Shear strength and deformation

of methane hydrate bearing sand with fines. In: Proceedings of the 18th International Conference on Soil Mechanics and Geotechnical Engineering, 1011–1014.

Hyodo, M., Li, Y.H., Yoneda, J., Nakata, Y., Yoshimoto, N., Nishimura, A., Song, Y.C., 2013a. Mechanical behavior of gas - saturated methane hydrate - bearing sediments. J. Geophys. Res.-Solid Earth. 118 (10), 5185-5194.

Hyodo, M., Nakata, Y., Yoshimoto, N., Ebinuma, T., 2005. Basic research on the mechanical behavior of methane hydrate-sediments mixture. Soils Found. 45 (1), 75-85

Hyodo, M., Hyde, A.F.L, Nakata, Y., Yoshimoto, N., Fukunaga, M., Kubo, K., Nanjo, Y., Matsuo, T. K. N., 2002. Triaxial compressive strength of methane hydrate. In: Proc. of 12th Int. Offshore and Polar Engrg. Conf. 422-428.

Itasca. Particle Flow Code in Three Dimensions (PFC3D), User's Manual, Version 5.0. Itasca Consulting Group, Minneapolis; 2015

Jager, M. D., Sloan, E. D., 2001. The effect of pressure on methane hydration in pure water and sodium chloride solutions. Fluid Phase Equilib. 185 (1), 89-99.

Jiang M.J., 2019. New paradigm for modern soil mechanics: Geomechanics from micro to macro, Huang Wenxi Lecture. Chinese Journal of Geotechnical Engineering, 41 (2), 195-254. (in Chinese)

Jiang, M.J., Liu, J., Shen, Z.F., 2019. DEM simulation of grain-coating type methane hydrate bearing sediments along various stress paths. Eng. Geol. 261, 105280, 1-13

Jiang, M. J., Jin, S. L., Shen, Z. F., Liu, W., Coop, M. R., 2015. Preliminary experimental study on three-dimensional contact behavior of bonded granules. In: 2015

International Symposium on Geohazards and Geomechanics, IOP Conference Series: Earth and Environmental Science, 26, 012007. doi: http://dx.doi.org/10.1088/1755-1315/26/1/012007.

Jiang, M.J., Shen, Z.F., Wang, J.F., 2015. A novel three-dimensional contact model for granulates incorporating rolling and twisting resistances. Comput. Geotech. 65, 147-163

Jiang, M.J., Zhang, N., Cui, L., Jin, S.L., 2015. A size-dependent bond failure criterion for cemented granules based on experimental studies. Comput. Geotech. 69, 182-198.

Jiang, M.J., Zhang, F.G., Sun, Y.G., 2014. An evaluation on the degradation evolutions in three constitutive models for bonded geomaterials by DEM analyses. Comput. Geotech. 57, 1-16.

Jiang, M.J., Zhu, F.Y., Liu, F., Utili, S., 2014. A bond contact model for methane hydrate - bearing sediments with interparticle cementation. Int. J. Numer. Anal. Methods Geomech. 38 (17), 1823-1854.

Jiang, M. J., Sun, Y. G., Li, L. Q., Zhu, H. H., 2012. Contact behavior of idealized granules bonded in two different interparticle distances: An experimental investigation. Mech. Mater. 55, 1-15.

Jiang, M.J, Chen, H., Tapias, M., Arroyo, M., Fang, R., 2014. Study of mechanical behavior and strain localization of methane hydrate bearing sediments with different saturations by a new DEM model. Comput. Geotech. 57, 122-138.

Jiang, M.J, Zhu, F.Y, Utili, S., 2015. Investigation into the effect of backpressure on the mechanical behavior of methane-hydrate-bearing sediments via DEM analyses.

Comput. Geotech. 69, 551-563.

Jiang, M.J., He, J., Wang, J.F., Chareyre, B., Zhu, F.Y., 2016. DEM analysis of geomechanical properties of cemented methane hydrate–bearing soils at different temperatures and pressures. Int. J. Geomech. 16 (3), 04015087.

Jiang, M.J., Peng, D., Ooi, J. Y., 2017. DEM investigation of mechanical behavior and strain localization of methane hydrate bearing sediments with different temperatures and water pressures. Eng. Geol. 223, 92-109.

Jin, S. L., 2016 Three dimensional experimental and numerical study on micro- and macro- mechanical behaviors of structural sands. Ms Thesis, Tongji University, Shanghai, China. (in Chinese)

Jones, S. J., Chew, H. A., 1983. Effect of sample and grain size on the compressive strength of ice. Ann. Glaciol. 4, 129-132.

Jung, J. W., Santamarina, J. C., Soga, K., 2012. Stress‐strain response of hydrate‐bearing sands: Numerical study using discrete element method simulations. J. Geophys. Res.-Solid Earth. 117, B04202.

Jung, J., 2010. Gas production from hydrate-bearing sediments: Geo-mechanical implications, Ph.D thesis, Georgia Institute of Technology, Atlanta.

Kajiyama, S., Wu, Y., Hyodo, M., Nakata, Y., Nakashima, K., Yoshimoto, N., 2017. Experimental investigation on the mechanical properties of methane hydrate-bearing sand formed with rounded particles. J. Nat. Gas Sci. Eng. 45, 96-107.

Kato, A., Nakata, Y., Hyodo, M., Yoshimoto, N., 2016. Macro and micro behaviour of methane hydrate-bearing sand subjected to plane strain compression. Soils Found. 56

(5), 835-847

Kharrat, M., Dalmazzone, D., 2003. Experimental determination of stability conditions of methane hydrate in aqueous calcium chloride solutions using high pressure differential scanning calorimetry. J. Chem. Thermodyn. 35 (9), 1489-1505.

Kvenvolden, K. A., 1988. Methane hydrate—a major reservoir of carbon in the shallow geosphere? Chem. Geol. 71 (1-3), 41-51.

Lafond, P.G., Olcott, K.A., Sloan, E.D., Koh, C.A., Sum, A.K., 2012 Measurements of methane hydrate equilibrium in systems inhibited with NaCl and methanol. J. Chem. Thermodyn., 48, 1-6.

Li, Y., Zhao, H., Yu, F., Song, Y., Liu, W., Li, Q., Yao, H., 2012. Investigation of the stress–strain and strength behaviors of ice containing methane hydrate. J. Cold Reg. Eng. 26 (4), 149-159. (in Chinese)

Li, Y.H., Zhao, H.H., Yu, F., Song, Y.C., Liu, W.G., Li, Q.P., Yao, H.Y., 2012. Investigation of the stress–strain and strength behaviors of ice containing methane hydrate. J. Cold Reg. Eng. 26 (4), 149-159.

Liu, Z.C., Wei, H.Z., Peng, L., Wei, C.F., Ning, F.L., 2017. An easy and efficient way to evaluate mechanical properties of gas hydrate-bearing sediments: The direct shear test. J. Pet. Sci. Eng. 149, 56-64.

Lu, H. L., & Matsumoto, R., 2005. Experimental studies on the possible influences of composition changes of pore water on the stability conditions of methane hydrate in marine sediments. Mar. Chem. 93 (2-4), 149-157.

Li, Y.H., Liu, W.G., Zhu, Y.M., Chen, Y.F., Song, Y.C., Li, Q.P., 2016. Mechanical

behaviors of permafrost-associated methane hydrate-bearing sediments under different mining methods. Appl. Energy. 162, 1627-1632.

Maekawa, T., 2001. Equilibrium conditions for gas hydrates of methane and ethane mixtures in pure water and sodium chloride solution. Geochem. J. 35 (1), 59-66.

Malinverno, A., Goldberg, D. S., 2015. Testing short-range migration of microbial methane as a hydrate formation mechanism: Results from Andaman Sea and Kumano Basin drill sites and global implications. Earth Planet. Sci. Lett. 422, 105-114.

Masui, A., Haneda, H., Ogata, Y., Aoki, K., 2005. Effects of methane hydrate formation on shear strength of synthetic methane hydrate sediments. In: Proceedings of the 15th International Offshore and Polar Engineering Conference. Seoul, Korea, 364–369. https://doi.org/10.1063/1.1804617

Mimachi, H., Takeya, S., Gotoh, Y., Yoneyama, A., Hyodo, K., Takeda, T., Murayama, T., 2016. Dissociation behaviors of methane hydrate formed from NaCl solutions. Fluid Phase Equilib. 413, 22-27.

Miyazaki, K., Masui, A., Sakamoto, Y., Aoki, K., Tenma, N., Yamaguchi, T., 2011. Triaxial compressive properties of artificial methane‐hydrate‐bearing sediment. J. Geophys. Res.-Solid Earth. 116, B06102.

Miyazaki, K., Masui, A., Sakamoto, Y., Tenma, N., Yamaguchi, T., 2010. Effect of confining pressure on triaxial compressive properties of artificial methane hydrate bearing sediments. In: Proceedings of the 2010 Offshore Technology Conference. Houston, TX, USA, OTC20721, 1823–1831.

Moridis, G., Collett, T.S., Pooladi-Darvish, M., Hancock, S.H., Santamarina, C.,

Boswell, R., Kneafsey, T.J., Rutqvist, J., Kowalsky, M.B., Reagan, M.T., Sloan, E.D., Sum, A., Koh, C., 2011. Challenges, uncertainties, and issues facing gas production from gas-hydrate deposits. SPE Reserv. Eval. Eng. 14 (01), 76–112.

Nabeshima, Y., Takai, Y., Komai, T., 2005. Compressive Strength and Density of Methane Hydrate. In: Proc. 6th ISOPE Ocean Min. Symp. 199-202

Nabeshima, Y., Matsui, T., 2003. Static shear behaviors of methane hydrate and ice. In: Proc. 5th ISOPE Ocean Min. Symp. 156-9.

Petrovic, J. J., 2003. Review mechanical properties of ice and snow. J. Mater. Sci. 38 (1), 1-6

Petrovic, J. J., 1987. Weibull statistical fracture theory for the fracture of ceramics. Metall Trans A. 18 (11), 1829-1834.

Piramoon, H., Moraveji, M. K., Parvareh, A., Azimi, A., 2019. Experimental study of the formation of natural gas hydrates in the presence of NaCl and KCl. Pet. Sci. Technol. 37 (17), 1924-1930.

Priest, J. A., Best, A. I., Clayton, C. R., 2005. A laboratory investigation into the seismic velocities of methane gas hydrate‐bearing sand. J. Geophys. Res.-Solid Earth. 110 (B4), 1–13

Santamarina, J. C., Dai, S., Terzariol, M., Jang, J., Waite, W. F., Winters, W. J., Nagao, J., Yoneda, J., Konno, Y., Fujii, T., Suzuki, K., 2015. Hydro-bio-geomechanical properties of hydrate-bearing sediments from Nankai Trough. Mar. Pet. Geol. 66, 434-450

Shen, Z.F., Jiang, M.J., Wan, R., 2016. Numerical study of interparticle bond failure by

3D discrete element method. Int. J. Numer. Anal. Methods Geomech. 40 (4), 523-545.

Shen, Z.F., Jiang, M.J., Thornton, C., 2016. DEM simulation of bonded granular material. Part I: contact model and application to cemented sand. Comput. Geotech. 75, 192-209.

Shen, Z.F., Jiang, M.J., 2016. DEM simulation of bonded granular material. Part II: extension to grain-coating type methane hydrate bearing sand. Comput. Geotech. 75, 225-243.

Sloan, E. D., 1998. Gas hydrates: review of physical/chemical properties. Energy Fuels. 12 (2), 191-196.

Sloan, E. D., 2003. Fundamental principles and applications of natural gas hydrates. Nature. 426 (6964), 353.

Sloan, E. D., Koh, C. A., 2008. Clathrate hydrates of natural gases. Third Edit.; CRC Press: Boca Raton, Florida, USA.

Soga, K., Lee, S. L., Ng, M. Y. A., Klar, A., 2006. Characterisation and engineering properties of methane hydrate soils. In: Proceedings of the 2nd International Workshop on Characterization and Engineering Properties of Natural Soils, Singapore. 4, 2591-2642.

Song, Y.C, Yu, F., Li, Y.H., Liu, W.G., Zhao, J.F., 2010. Mechanical property of artificial methane hydrate under triaxial compression. J. Nat. Gas Chem. 19 (3), 246-250.

Stern, L. A., Lorenson, T. D., 2014. Grain-scale imaging and compositional characterization of cryo-preserved India NGHP 01 gas-hydrate-bearing cores. Mar. Pet.

Geol. 58, 206-222.

Sultan, N., Cochonat, P., Foucher, J. P., Mienert, J., 2004. Effect of gas hydrates melting on seafloor slope instability. Mar. Geol. 213(1-4), 379-401.

Sylva, T. Y., Kinoshita, C. K., Masutani, S. M., 2016. Inhibiting effects of transition metal salts on methane hydrate stability. Chem. Eng. Sci. 155, 10-15.

Sun, S. C., Liu, C. L., Ye, Y. G., Jiang, Q., 2011 Dissociation conditions and influencing factors of methane hydrate in chloride salt solution under high pressure. Acta Phys.-Chim. Sin. 27 (12), 2773-2778. (in Chinese)

Thornton, C., 2000. Numerical simulations of deviatoric shear deformation of granular media. Géotechnique. 50 (1), 43-53.

Uchida, S., Soga, K., Klar, A., Yamamoto, K., 2012. Geomechanical study of the Mallik gas hydrate production field trials. Bull. Geol. Surv. Can. 601, 191-204.

Vinod, J. S., Hyodo, M., Indraratna, B., Miller, R., 2014. DEM modeling of methane hydrate bearing sand. Aust. Geomech. J. 49 (4), 175-182

Waite, W.F., Winters, W.J., Mason, D.H., 2004. Methane hydrate formation in partially water-saturated Ottawa sand. Am. Miner. 89 (8–9), 1202–1207

Waite, W. F., Santamarina, J. C., Cortes, D. D., Dugan, B., Espinoza, D. N., Germaine, J., Jang, J., Jung, J.W., Kneafsey, T.J., Shin, H., Soga, K., Winters, W.J., Yun, T.S., 2009. Physical properties of hydrate - bearing sediments. Rev. Geophys. 47 (4), 1-38.

Wang, Q., Tang, Q., Tian, S., 2020. Molecular dynamics simulation of sI methane hydrate under compression and tension. Cent. Eur. J. Chem. 18 (1), 69-76.

Weibull, W., 1939. A statistical theory of strength of materials, IVA Handlingar No.151.

Proc. Roy. Swed. Acad. of Eng. Sci. 1-45.

Winters, W. J., Wilcox-Cline, R. W., Long, P., Dewri, S. K., Kumar, P., Stern, L., Kerr, L., 2014. Comparison of the physical and geotechnical properties of gas-hydrate-bearing sediments from offshore India and other gas-hydrate-reservoir systems. Mar. Pet. Geol. 58, 139-167.

Winters, W.J., Pecher, I.A., Waite, W.F., Mason, D.H., 2004. Physical properties and rock physics models of sediment containing natural and laboratory-formed methane gas hydrate. Am. Miner. 89, 1221–1227.

Xiao, Y., Liu, H.L., Sun, Y.F., Liu, H., Chen, Y.M., 2015. Stress–dilatancy behaviors of coarse granular soils in three-dimensional stress space. Eng. Geol. 195, 104-110.

Yu, F., Song, Y.C., Liu, W.G., Li, Y.H., Zhao, J.F., 2010. Study on shear strength of artificial methane hydrate. In: Proc. Int. Conf. Offshore Mech. Arct. Eng. 705-710, DOI: 10.1115/OMAE2010-21174.

Yun, T. S., Santamarina, J. C., Ruppel, C., 2007. Mechanical properties of sand, silt, and clay containing tetrahydrofuran hydrate. J. Geophys. Res.-Solid Earth. 112, B04106.